This is a preprint, the final version is subject to change, of the American Mineralogist (MSA)
Cite as Authors (Year) Title. American Mineralogist, in press.
(DOI will not work until issue is live.) DOI: http://dx.doi.org/10.2138/am-2016-5524

Revision 2

Dissolution-reprecipitation metasomatism and growth of zircon within phosphatic garnet in metapelites from western Massachusetts

Emily M. Peterman[1], David R. Snoeyenbos[2], Michael J. Jercinovic[2], Andrew Kylander-Clark[3]

[1]Earth and Oceanographic Science, Bowdoin College, 6800 College Station, Brunswick, ME 04011

[2]Dept. of Geosciences, Univ. of Massachusetts, Amherst, 611 N. Pleasant Street, Amherst, MA 01003

[3]Dept. of Earth Science, Univ. of California, Santa Barbara, Webb Hall, Santa Barbara, CA 93106-9630

ABSTRACT

Highly restitic garnet-kyanite-phlogopite metapelitic schists from the Goshen Dome of western Massachusetts contain: a population of prograde monocrystalline, megacrystic garnet, some with significant P in substitution for Si; precipitates of hydroxylapatite and rutile; and <1μm zircon crystals of undetermined origin and abundance on the order of $10^5/mm^3$. The unusual P content and the abundant internal precipitate suite are similar to features reported in garnet from ultrahigh-pressure (UHP) and mantle settings, suggesting a potential (U)HP origin for the garnet megacrysts. Zircon included in megacrysts is surrounded by radial fractures, indicating in situ volumetric expansion or new growth. Cores display rare earth element (REE) profiles and cathodoluminescence (CL) zoning consistent with magmatic growth, and yield only Paleozoic dates (447–404 Ma). The embayed core-rim boundary is marked by a several μm wide band of CL-dark zircon enriched in Y, P, U, and Th that is interpreted as the accumulation of redistributed xenotime component from the original zircon rim during metamorphism. Outside of this band, the rim has elevated Hf, Th/U<<1, and steep heavy REE profiles. The metamorphic rims yield concordant dates from 400 to 381 Ma. Matrix zircon grains have magmatic cores (1726–415 Ma) with similar core–rim boundaries enriched in Y, P, U, and Th. Metamorphic rims on matrix zircon yield slightly younger dates (393–365 Ma) and are compositionally heterogeneous.

The difference between the youngest core and oldest rim indicates a short interval (c. 4 Ma) between deposition of detrital zircon and the onset of metamorphism in the earliest Acadian.

The oldest zircon rim dates are found within phosphatic garnet megacrysts of possible very high-pressure origin. The compositional uniformity of these rims indicates equilibrium with a single source; the anomalous composition suggests a combination of dissolution-reprecipitation and new growth of zircon that is derived from garnet. The range in both composition and dates indicate that matrix zircon rims formed in response to local changes in mineralogy and fluid/melt composition and/or availability. New growth of zircon on these grains cannot be confirmed, suggesting that dissolution-reprecipitation reactions during continued metamorphism may be the dominant mechanism that formed these rims. The data collectively suggest that dissolution-reprecipitation may be a common mechanism for producing metamorphic rims on zircon that does not require additional Zr and Hf, which are limited within most metamorphic settings.

Keywords: zircon, garnet, LASS, dissolution-reprecipitation, metasomatism, metamorphism

INTRODUCTION

Although the diffusion rate of Pb in geochronologic minerals, such as zircon and monazite, is slow under most geologic conditions (Cherniak and Watson 2001; Cherniak et al. 2004), the distribution of radiogenic Pb—crucial to U-Th-Pb geochronology—can be affected by several mechanisms during metamorphic or thermal events. Recent studies by secondary ionization mass spectrometry (SIMS—Kusiak et al. 2013) and atom probe tomography (APT) demonstrate that short-range diffusion on reheating can cause Pb atoms in zircon (Valley et al. 2015) and monazite (Snoeyenbos et al. 2013) to aggregate with various other ions in radiogenic damage spots in the crystal lattice. The bulk composition of a crystal—including the Pb distribution—may be modified along a reaction front propagating through a crystal via a dissolution-reprecipitation reaction. In zircon (Geisler et al. 2007; Rubatto et al. 2008; Hay and Dempster 2009; Harlov et al. 2012), xenotime (Harlov and Wirth 2012), and monazite (Harlov et al. 2011; Williams et al. 2011), dissolution-reprecipitation reactions are mediated by an alkali-bearing intergranular fluid that enables complete removal of radiogenic Pb, thus resetting the radiometric age along a reaction front that propagates into the crystal. Other compositional changes (e.g. accumulation of Th, U or decreases in other minor and trace elements) may also occur along the reaction front (Tomaschek et al. 2003; Geisler et al. 2007; Rubatto et al. 2008), but detailed study is required to fully explain these reactions.

Dissolution-reprecipitation reactions commonly affect only a portion of the crystal, thereby leaving metasomatized, geochronologically-reset concordant domains adjacent to unreacted concordant domains (Schwartz et al. 2010). In many cases, the texture, radiometric age, and chemical composition produced by the propagation of dissolution-reprecipitation reactions in zircon and monazite can appear similar to metamorphic or igneous overgrowths on an inherited core (Rubatto et al. 2008; Vonlanthen et al. 2012). Because conditions favoring metasomatism by dissolution-reprecipitation—e.g. changes in pressure-temperature (P-T) conditions, changes in fluid activity, and the availability and diffusivity of components—overlap with conditions of metamorphic overgrowth as conventionally understood, both processes may occur simultaneously and may be initiated under similar conditions. Identification of the relative contribution of each of these mechanisms to the formation of a metamorphic rim requires integration of compositional, textural, and geochronologic information.

We present a case study of two zircon populations that have been examined in detail via in situ electron probe microanalysis (EPMA), laser ablation split stream (LASS) inductively coupled plasma mass spectrometry (ICPMS), and cathodoluminescence (CL) imaging. The first population (herein referred to as zircon1) consists of zircon included in phosphatic garnet megacrysts within coarse garnet-kyanite-phlogopite schist. Elevated P and the precipitate suite included in garnet suggest preservation of potentially very high-pressure metamorphism. The second zircon population (herein referred to as zircon2) is included in the recrystallized phlogopite, kyanite, quartz, and non-phosphatic garnet matrix surrounding these megacrysts. Both zircon populations exhibit embayed core-rim boundaries marked by a thin CL-dark band that is enriched in U, Y, P, and Th. These components are interpreted to have been derived from the original zircon and were mobilized and localized along an inward-propagating dissolution-reprecipitation reaction front in response to metamorphism on a low-temperature/high-pressure path, as suggested by experimental work by Tomaschek (2010). The compositional and dates of zircon1 rims indicates equilibration with and derivation from a single source—the host garnet. Precipitation of zircon from garnet may also explain the myriad c. 1 μm zircon crystals found only within the garnet megacrysts. Compositional heterogeneity among zircon2 rims indicates response to local changes in mineralogy and fluid/melt composition and/or availability during protracted Acadian metamorphism.

SETTING

Multiple phases of orogenesis within the northern Appalachians have been documented (e.g. Robinson et al. 1998; Macdonald et al. 2014), but only two main phases are classically recognized in the Paleozoic assembly of western Massachusetts: (1) the west-directed Taconian accretion of the Shelburne Falls (or Bronson Hill) Arc against the Laurentian margin that began ca. 475-470 Ma (Karabinos et al. 1998), and (2) west-directed thrusting of Devonian metasediments and regional high-temperature metamorphism associated with the Acadian orogeny (Armstrong et al. 1992) over the previously accreted Taconian arc rocks. Monazite from regional schists suggests that the high-temperature metamorphism associated with the Acadian orogeny occurred between 390–350 Ma, with peak pressures attained at c. 370 Ma (Pyle and Spear, 2003; Pyle et al., 2005; Cheney et al., 2006). Garnet geochronology from the Townshend Dam in southern Vermont is broadly consistent with this timeframe and indicates prograde garnet growth from 383.1 ± 6.8 Ma (oldest garnet core) to 374.9 ± 1.8 Ma (youngest garnet rim) (Gatewood et al., 2015).

The Goshen Dome, located in western Massachusetts (**Fig. 1a**), has been mapped as a tectonic window through the Devonian Goshen Formation (interpreted as an Acadian thrust sheet) into core gneisses and associated rocks (**Fig. 1b**) with unclear internal relations (Hatch and Warren, 1981). Central to the structure is the poorly exposed Collinsville Gneiss, which yielded a U-Pb zircon date of 473 ± 2 Ma that has been interpreted as the timing of igneous activity (Karabinos et al. 1998). The overlying Cobble Mountain Formation on the western side of the Dome contains a novel package of high-grade rocks originally described by O'Brien and Koziol (2008) as granulite facies assemblages. Subsequent study of garnet chemistry reinterpreted the garnet megacrysts within this unit as potentially ultrahigh-pressure (UHP) relics (Snoeyenbos et al., 2011). This heterogeneous package of rocks consists of numerous complexly folded and boudinaged migmatitic garnet amphibolites and kyanite schists, and restitic, coarse-grained, garnet-kyanite-phlogopite schists. The coarse-grained, schists contain multiple garnet populations that range from 0.5 to 8 cm in diameter. These coarse-grained schists crop out as sheets several meters thick associated with highly strained rocks of lower metamorphic grade.

SAMPLE DESCRIPTIONS

Four garnet-kyanite-phlogopite schists were sampled from the anomalous package of rocks located within the Cobble Mountain Formation **(Fig. 1b)**. Two of the samples (RBTS and

WMBTS) were collected from different exposures of coarse-grained schist. Three garnet megacrysts were analyzed for this study: two specimens from RBTS, herein referred to as RBTS (**Figs. 2-3**) and RBTS-B (**Fig. 4**), and one specimen from WMBTS (**Fig. 5**). Garnet megacrysts in RBTS are >3 cm in diameter with rounded and partially resorbed margins. The megacryst from WMBTS is a 3 cm diameter, equant, euhedral garnet (**Fig. 5a**) with a light pink core and a dark purple rim. Zircon1 is found within these phosphatic garnet megacrysts. Two samples that lack garnet megacrysts, G12B and G12G, were collected from different schists composed mainly of non-phosphatic garnet, quartz, kyanite, cordierite, phlogopite, chlorite, and rutile. Zircon2 is found in G12B, G12G, and in the matrix surrounding the garnet megacryst in WMBTS.

Garnet-megacryst-bearing samples (RBTS, WMBTS)

RBTS is located at the northern end of the exposure of the anomalous package of rocks (**Fig. 1b**). WMBTS is 10 m structurally below RBTS and 2 m above the lower bounding shear zone (**Fig. 1b**). These samples are principally composed of phosphatic garnet, kyanite, quartz, phlogopite, plagioclase, cordierite, rutile, and ilmenite, with minor chlorite associated with retrograde metamorphism. Zircon and apatite are found throughout the samples; monazite is found in all contexts except within the pristine garnet megacryst in WMBTS.

Doubly-polished, thick (100 μm) petrographic sections were prepared for studying the inclusion suites in the garnet megacrysts because they contain a larger volume of material than standard preparations and allow investigation of inclusions and precipitates in three dimensions. All three phosphatic garnet specimens—RBTS, RBTS-B, and WMBTS—have Mn- and Ca-rich cores, and Mg# increases systematically from core to rim, consistent with prograde growth. The notable smoothness of the Mn profiles indicates some diffusional relaxation. At the rim and along fractures, the elevated Mn distribution and external morphology record minor resorption. Another distinctive feature of the phosphatic garnet megacrysts is extremely low O-isotope ratios, at least in specimen RBTS. The $\delta^{18}O$ of the core measured by secondary ion mass spectrometry (SIMS) is as low as 2.0 ‰, with fractionation to 3.0 ‰ at the rim (Russell 2012; specimen RBTS is designated 'CH-2' in that work). Such values and profiles are similar to eclogitic and known UHP garnet (Russell 2012).

Garnet megacrysts contain abundant sub-μm hydroxylapatite inclusions, as identified by confocal Raman. These inclusions are anhedral blebs disposed along linear to slightly helical trails normal to the garnet crystal faces and sub-parallel within each sector of the megacryst. The arrangement of apatite inclusion trails by sector is especially apparent in WMBTS (**Fig. 5a**) but may also be discerned in RBTS (**Fig. 2a**). The density of apatite inclusions is greatest in the high-Ca cores of these specimens. Their disposition along curvilinear trails recalls that of precipitates in high-pressure garnet described by van Roermund et al. (1999), who interpreted such precipitate trails as having formed along un-annealed growth dislocations in the garnet lattice. The apatite trails are closely associated with fine (sub-μm) rutile needles in the garnet in several parallel orientations.

The distribution of intrinsic P in specimen RBTS (**Fig. 2d**) is low (ca. 0.03 wt% P_2O_5) in the high-Ca, hydroxylapatite inclusion-rich core, but considerably higher (locally >0.10 wt% P_2O_5) in the low-Ca garnet zone surrounding the high-Ca core, where hydroxylapatite inclusions are distinctly less abundant. The relationship between Ca content and the distribution of hydroxylapatite inclusions is accentuated in specimen RBTS-B. Specimens RBTS and RBTS-B have nearly the same major element compositional profiles, but unusually among these garnet megacrysts, a portion of the low-Ca mantle region of RBTS-B is almost entirely free of fine inclusions (**Fig. 4**). This region of specimen RBTS-B has intrinsic P up to 0.22 wt% P_2O_5 and few fine hydroxylapatite inclusion trails. The corresponding part of specimen RBTS has only up to 0.14 wt% P_2O_5, but the garnet is clouded by sub-μm hydroxylapatite trails and rutile inclusions.

Other apparent precipitates within garnet RBTS are rutile blades up to 200 μm long and only a few μm thick. Many of them are twinned, some of them 'butterfly' twins, whereas others are co-planar (**Fig. 3c**). Rutile twins range in color from pale brown to violet and blue. Locally, clusters of thin zircon blades up to 30 μm long are found. Micrometer to sub-μm subhedral to euhedral zircon crystals are observed throughout garnet specimen RBTS with a density of ca. $10^3/mm^2$ **(**white flecks in **Fig. 3b**), or ca. 10^7 such zircons over the area of the RBTS garnet in thin section. The dimensions of the zircon blades and micro-crystals present a challenge for analysis by EPMA, and their minor element compositions and Hf/Zr signatures are as yet unknown. Zircon inclusions of detrital origin (25 to 100 μm) are distributed throughout the garnet megacryst in RBTS, nearly all of which are surrounded by shattered garnet (**Fig. 3b**). Epidote inclusions (~20 μm) occur along late penetrative fractures. The dark pink rim domain contains mm-scale rutile and ilmenite grains that are oriented parallel to garnet growth faces. Millimeter-scale monazite grains decorate the outer 1 cm of the megacryst, but monazite is not found within the core of the garnet. There are no primary quartz inclusions in the megacryst.

Specimen WMBTS contains a suite of inclusions and precipitates identical to that in specimen RBTS, with the exception of the zircon blades and monazite near the rim. This specimen lacks penetrative fractures with epidote and other alteration products. Specimen WMBTS retains little intrinsic P in the garnet, but the abundant hydroxylapatite precipitate trails are interpreted to reflect an elevated original P content. Among the three garnet megacrysts presented here, significant intrinsic P is found mainly where X_{Grs} <0.03. Elevated intrinsic P is not found in specimen WMBTS, but the Ca content is not below X_{Grs}=0.06, even in the low-Ca mantle.

The unusual P content of the garnet megacrysts in this study (up to at least 0.22 wt% P_2O_5), together with their abundant internal precipitates of apatite and rutile, invite close comparison with similar features reported in garnet from ultrahigh-pressure (UHP) and mantle settings (Haggerty et al. 1994; Ye et al. 2000; Mposkos and Kostopoulos 2001; Ruiz Cruz and Sanz de Galdeano 2013). However, in the present example, the phosphatic garnet does not contain free SiO_2 inclusions, as might be expected for typical garnet in metapelites, nor has any free C yet been found either in the garnet or in matrix, so detection of conventional UHP minerals remains problematic at this locality.

The matrix surrounding these garnet megacrysts is composed of recrystallized quartz, phlogopite, kyanite, cordierite, plagioclase, and chlorite, with zircon, apatite, and monazite as accessory phases. Smaller matrix garnet grains (mm- to cm-scale) lack the distinctive hydroxylapatite and rutile precipitates that are abundant in the megacrysts and have an inclusion suite that is principally composed of mm-scale rutile, ilmenite, quartz, and phlogopite. Kyanite and cordierite are poikiloblastic, and cordierite commonly surrounds decomposed kyanite. Matrix-hosted zircon and monazite measure <100 μm and are typically aligned with the fabric. The fabric wraps around the megacryst, but cordierite and kyanite are typically aligned with the foliation.

Matrix samples (G12B, G12G)

Sample G12B is located 3 m south from the sample location for RBTS (**Fig. 1b**). This sample contains garnet with three different morphologies and inclusion arrays. The largest garnet grains (>1cm) have curved inclusion trails of rutile and ilmenite. These grains do not typically have primary quartz or phlogopite inclusions. Although some smaller garnet grains (<1 cm) are relatively pristine with a few 10-100 μm-scale rutile + ilmenite + quartz ± phlogopite inclusions, many garnet grains are skeletal with mm-scale quartz and rutile inclusions. All garnet is rimmed by chlorite, phlogopite, quartz ± cordierite ± kyanite (**Fig. 6**). Kyanite exhibits three different textures: 1) subhedral cm-scale grains with embayed margins, 2) deformed cm-scale grains with undulatory extinction, and 3) skeletal fragments of cm-scale porphyroblasts rimmed by cordierite (**Fig. 6**). Rutile inclusions are abundant in all kyanite grains. The coarse-grained matrix is comprised of phlogopite, chlorite, and quartz with decomposed kyanite and minor plagioclase (**Fig. 6d**). Sillimanite and andalusite are absent, whether as replacement textures or pseudomorphs. Quartz is abundant in the matrix; vein quartz is commonly present as large (up

This is a preprint, the final version is subject to change, of the American Mineralogist (MSA)
Cite as Authors (Year) Title. American Mineralogist, in press.
(DOI will not work until issue is live.) DOI: http://dx.doi.org/10.2138/am-2016-5524

to 20cm) boudins of cm-scale crystals. Rutile and ilmenite are concentrated in the chlorite + phlogopite ± garnet domains and largely absent from the recrystallized quartz domains. The fabric wraps around both garnet and kyanite domains. Zircon, apatite, and monazite are abundant in both the matrix and the porphyroblasts.

Sample G12G is located 10 m structurally below RBTS and G12B (**Fig. 1b**). Thin sections from this sample are similar to G12B and typically contain a matrix of quartz + chlorite + plagioclase that wraps around cm-scale porphyroblasts of garnet, cordierite, and kyanite. Garnet contains mm-scale apatite inclusions and ~10 μm rutile needles that are oriented parallel to garnet crystal growth faces. Garnet is commonly rimmed by quartz, cordierite, and chlorite; mm-scale rutile grains in chlorite are abundant throughout the matrix. Cordierite contains abundant inclusions of kyanite, quartz, phlogopite, and chlorite. Kyanite is rimmed by cordierite, chlorite, and phlogopite. Zircon, apatite, and monazite are abundant in both the matrix and the porphyroblasts.

METHODS

Zircon included in garnet megacrysts from WMBTS and RBTS and in the matrix for G12B, G12G and WMBTS were imaged by cathodoluminescence (CL) and mapped by electron microprobe analysis (EPMA). Quantitative EPMA and laser ablation split stream (LASS) inductively coupled plasma mass spectrometry (ICPMS) data were also collected from representative zircon and garnet in these samples.

Scanning Electron Microscope (SEM) Analysis

Zircon grains were located in situ using backscattered electron (BSE) imaging and energy dispersive X-ray spectroscopy (EDS) on the LEO 1450VP Scanning Electron Microscope (SEM) at Bowdoin College. Panchromatic CL images were collected using a Centaurus CL detector attached to an FEI Quanta 400F field emission SEM (UC Santa Barbara) and a TESCAN CL detector attached to a TESCAN Vega3 SEM that uses a LaB6 source (Boston College). Both instruments were operated at 10.0 kV and a beam current that was optimized for each instrument (between 77 and 100 pA).

Electron Probe MicroAnalysis (EPMA)

Quantitative compositional analysis and mapping of zircon and garnet were performed on the CAMECA SX-50 and SX-UltraChron instruments at the University of Massachusetts. Mapping and major and minor element analysis of garnet were done on the SX-50 at 15 kV and beam current of 200nA (mapping) and 40 nA (analysis). Zircon mapping and analysis, and trace element analysis of garnet were done on the Cameca SX-UltraChron EPMA at 300nA (mapping) and 200 nA (analysis). Minor and trace element quantitative analysis was performed using Probe for EPMA software (Probe Software, Inc.) and included the use of multi-point backgrounds, multiple spectrometer count integration, extended count times (100 to 600 sec), and matrix-iterated interference corrections. Large and very large PET (LPET and VLPET) monochromators were utilized as appropriate.

Laser Ablation Split Stream (LASS) Analysis

Largely following the methods of Kylander-Clark et al. (2013), polished sections and reference material mounts were loaded in a Photon Machines HelEx cell connected to a Photon Machines 193 nm excimer laser at the LASS Facility at UC Santa Barbara. The HelEx cell was purged with He gas; a combination of He and Ar carrier gases swept the ablated material through Teflon tubing to a T-junction where the analyte was split into two streams that were measured simultaneously—one stream was measured on the Nu Plasma multi-collector ICPMS for U-Pb isotopes; the other stream was measured on the Nu AttoM single-collector ICPMS for Ti, Y, Hf, and rare earth elements (REE). Prior to analysis, each spot was cleaned with two laser pulses to remove surface contaminants and/or residual material from an adjacent analysis. Zircon was analyzed at 15, 20 and 24 μm spot sizes. Operating conditions (e.g. gas flows, laser energy) were optimized for each spot size and produced laser pit depths <8 μm. Analyses were conducted following traditional sample–RM bracketing protocols to correct for bias and drift of the instrument (e.g. Kylander-Clark et al. 2013).

91500 (1062.4 ± 0.4 Ma; Wiedenbeck et al. 1995) and GJ1 (Jackson et al. 2004) were used as primary RMs for age and composition, respectively. The specific piece of GJ1 used in these is 601.7 ± 1.3 Ma ($^{206}Pb/^{238}U$ date; Kylander-Clark et al. 2013). Plešovice (337.13 ± 0.37 Ma; Slama et al. 2008) was also analyzed as a secondary RM. Over a two-day analytical session, Plešovice yielded a $^{206}Pb/^{238}U$ date of 340.3 ± 0.8 Ma (MSWD = 1.2, n = 40) and GJ1 yielded a $^{206}Pb/^{238}U$ date of 605.6 ± 1.2 Ma (MSWD = 0.86, n = 61). These uncertainties represent internal uncertainties only and are not propagated for systematic biases. Each analytical run began with a block of 8 analyses on the RMs. The RM block was followed by blocks of 5 to 8 measurements on unknowns and 2 RM measurements. At the end of the run, a second block of 8 analyses on the RMs was measured. Ratios were bias, drift, and age corrected using *Iolite* (Paton et al. 2010) following procedures detailed in Kylander-Clark et al. (2013). Although the uncertainty on an individual ratio was typically <1% (2σ), the long-term reproducibility of secondary RMs is c. 1.5% (2σ) and is attributed to variation in laser energy and gas flow within the cell (Kylander-Clark et al. 2013). Therefore, to account for measurement uncertainty, the assumed uncertainty in the age of the RM, and the long-term reproducibility of the RMs analyzed, we conservatively assign 2% uncertainty (2σ) to unknown analyses to enable comparison among analytical sessions.

RESULTS

Zircon grains imaged via CL reveal zoning patterns and guide locations for wave dispersive spectrometry (WDS) and LASS analysis. The cores of zircon1 exhibit oscillatory zoning in CL (**Fig. 7a**). Approximately half of the zircon1 cores are broken by fractures that displace zircon fragments by ca. 5–10 μm (**Fig. 7b**). Many zircon1 cores have distinctly scalloped or embayed margins that crosscut the oscillatory zoning; other cores preserve a subhedral to euhedral outline.

Regardless of position within the garnet megacryst, all zircon1 cores (including their isolated or displaced fragments) are surrounded by a distinctive and complex rim ca. 2–10 μm in width.

Within this rim, a band of CL-dark zircon up to several μm thick is located immediately adjacent to the core, often with lobate boundaries. Surrounding this CL-dark band, the rims of nearly all zircon1 are characterized by complex zoning patterns that are dominantly CL-bright (**Fig. 7a-b**). The external margins of these metamorphic rims are typically curved to lobate. All zircon1 grains are surrounded by radial fractures that extend up to 100 μm into the garnet (**Fig. 3d-e**) and mainly originate from lobes and protrusions in the periphery of the zircon1 grains.

Most zircon2 grains are subhedral; a few grains are octahedral (see Data Supplement Figure 1). The cores of zircon2 typically exhibit oscillatory zoning in CL. All cores are mantled by a CL-dark band (**Fig. 8**) and most rims have complex CL-bright domains that vary greatly in CL brightness, zoning and width (1 to 20 μm). Beyond the CL-bright domain, many rims are CL-dark to the edge of the grain (**Fig. 8c**). Although a few zircon2 grains are fractured, no metamorphic rims formed post-fracturing. None of the grains exhibit radial fractures extending into the host mineral.

Mapping by EPMA reveals that the cores of nearly all zircon grains in both populations have minor Hf variation (**Figs. 7, 8**), which is consistent with primary igneous zonation (e.g. Corfu et al. 2003). Some zircon2 apparently lack this core (see Data Supplement Figure 1), but these may represent low-angle cuts through the rim that did not intersect the core. The thin CL-dark band is strongly enriched in Th, U, P, and Y (**Fig. 7a-b, 8**). Within this band, Th is enriched immediately adjacent to the unreacted core, mainly in an envelope less than 100 nm thick, as determined by APT; the width of U-enrichment is broader than that of Th (Snoeyenbos et al.

2012). The elevated P and Y in the CL-dark domains are spatially covariant, reflecting enrichment in the xenotime component. WDS mapping also reveals a monotonic intensity of Hf Mα from the inner margin of the rim to the outer margin of the grain (**Fig. 7**), despite CL and/or minor element zonation measured in the complex rim.

Within zircon1, quantitative analysis reveals that core compositions vary widely in HfO_2 and ThO_2 (color-filled symbols, **Fig. 9a-b; Table 1**; full analytical results in Data Supplement Table 1) whereas the rims are nearly uniform (white-filled symbols, **Fig. 9a-b; Table 1**). Outside of the Th-rich inner band, the rims are enriched in HfO_2 and devoid of ThO_2. The rim compositions show remarkable large-scale grain-to-grain uniformity within each garnet and do not correlate with the composition of the zircon core or the location within the garnet (**Fig. 9a-b**). The core compositions in zircon2 also vary widely in HfO_2, but the mean compositions of the core and rim overlap (**Table 1**) and the rim compositions vary considerably among grains (**Fig. 9c**).

The cores of zircon1 analyzed via LASS ICPMS analysis yielded ^{207}Pb-corrected ^{206}Pb/^{238}U dates that range from c. 447 to 404 Ma (± 2%, 2σ) (**Table 2**). Chondrite-normalized REE patterns measured from the cores (green lines, **Fig. 10a**) show a positive Ce anomaly, a negative Eu anomaly, and high heavy rare earth element (HREE) concentrations with a positive slope, consistent with magmatic growth (gray field, **Fig. 10a**; adapted from Hoskin and Ireland 2000; Hoskin and Schaltegger 2003). The Th/U of these analyses varies from 0.3 to 1.2 (**Fig. 10b**).

The rims of zircon1 yield LASS ICPMS ^{207}Pb-corrected ^{206}Pb/^{238}U dates that range from 401 to 373

Ma (± 2%, 2σ) (black lines, **Fig. 10a; Table 2**). Most rim analyses lack a positive Ce anomaly and have a shallow Eu anomaly. The slope of the HREE is significantly steeper than the analyzed cores; the slope is primarily attributed to middle rare earth element (MREE) depletion, rather than HREE enrichment. The Th/U ratio of these spots is less than 0.05 (**Fig. 10b**). Older rim analyses (c. 530 to 450 Ma; **Table 2**) are analytically concordant, but have high common-Pb (dashed lines in **Fig. 10a**) and yield low Th/U (<0.02; **Table 2**). Two rim analyses from zircon1 yield younger dates (373 and 377 Ma), Th/U >0.2 (blue circles, **Fig. 10b**), and REE patterns consistent with magmatic growth (blue lines, **Fig. 10a; Table 2**).

Because LASS analysis yields pits up to 8 μm in depth, some analysis volumes represent mixtures between core and rim compositions. Although highly discordant U-Pb analyses often indicate mixtures, a mixture of core and rim domains that are similar in age may appear concordant. In these cases, post-analysis imaging by EPMA can provide useful information for data interpretation, as shown in **Fig. 7 and 8**. Variations in specimen height on the order of the laser pit depth (<8 μm) do not prevent acquisition of useful qualitative EPMA intensity data, and the 40° takeoff angle of the spectrometers provides imaging of portions of the pit walls. For example, the Hf and U maps of the zircon grain in **Fig. 7a** show that the discordant analysis marked in red (454 Ma) sampled through the zircon and into the garnet. The concordant spot marked in orange (393 Ma) was placed to sample only the core observed in CL, but the analysis penetrated down through the core and into the high-Hf rim, as seen on the Hf map (**Fig. 7a**). Further, as implied by the Hf map and confirmed by the U map, this LASS analysis sampled the CL-dark U-rich dissolution-reprecipitation reaction front between core and rim and yet yielded a concordant date. The rims for this grain yield older dates than the cores (black; **Fig. 7a**), but the analyses have high common Pb.

Zircon2 grains yield ^{207}Pb-corrected ^{206}Pb/^{238}U dates that range broadly from 1726 to 365 Ma (**Fig. 11**), most of which are analytically concordant (**Table 2;** See Data Supplement Table 2). The uncertainty ranges from 8 to 30 Ma, which is largely dependent on the date and the reproducibility of the RM. All analyses <400 Ma yield low Th/U (**Fig. 11b**).

The youngest concordant date from the core of a zircon2 grain is 415 Ma. The REE patterns of core analyses from zircon2 (green lines, **Fig. 11a**) are consistent with magmatic growth. They have steep HREE patterns, a positive Ce anomaly and a negative Eu anomaly. The Th/U ratios vary broadly (**Fig. 11; Table 2**), but most analyses of cores yield Th/U greater than 0.1.

The dates of zircon2 rims vary, but the concordant analyses are all <400 Ma. Half of the rim analyses yield flat to convex-up HREE patterns (black lines, **Fig. 11a**), which are consistent with growth during garnet stability (e.g. Rubatto 2002; Hoskin and Schaltegger 2003) and are compatible with the HREE composition of garnet measured in these samples (see Data Supplement Table 3). The other analyses yield HREE patterns similar to zircon2 cores (**Fig. 11a**). Nearly all analyses yield positive Ce and negative Eu anomalies and Th/U less than 0.1 (**Fig. 11b**). There are no correlations between the host phase (e.g. cordierite, chlorite, kyanite) and the zircon REE composition; the zircon date and its REE composition; or the host phase and the zircon date.

Although two zircon2 rims yield concordant dates (434 and 405 Ma), post-analysis imaging indicates that these LASS analyses partially sampled the older core. In samples where the difference in age between core and rim domains is small, results from mixed domains such as these can be analytically concordant, but they mix isotopic ratios from the two domains, so they should not be used to constrain the timing of metamorphism.

INTERPRETATIONS

Garnet megacrysts

One of the most distinctive features of the phosphatic garnet megacrysts is their abundant sub-μm inclusions of hydroxylapatite and rutile. In thin section, these inclusions are arranged by sector in the host crystal, with the hydroxylapatite blebs in curvilinear trails normal to the sector face, and the coexisting rutile needles in several crystallographic orientations. Anti-correlation between the sub-μm hydroxylapatite inclusions and locally high intrinsic P in the garnet megacryst specimens presented here supports the interpretation that the sub-μm hydroxylapatite are precipitates from garnet compositions that were originally as high as 0.22 wt% P_2O_5.

Elevated P in garnet is well known from several HP/UHP crustal examples such as the Erzgebirge in the Bohemian Massif, 0.4 wt% P_2O_5 (Axler and Ague, 2015); the Kimi Complex of the Rhodope Massif, 0.33 wt% P_2O_5 (Mposkos and Kostopoulos 2001); the northern Rif, 0.12 wt% P_2O_5 (Ruiz Cruz and Sanz de Galdeano 2013); and from mantle eclogites, 0.13 wt% P_2O_5 (Haggerty et al. 1994). In the crustal examples, hydroxylapatite and rutile ± ilmenite precipitates are also reported. The apparent exclusive analogy between the P content and hydroxylapatite precipitates in garnet from the Goshen Dome locality and several diamond-bearing crustal UHP occurrences, suggests that these phosphatic garnet megacrysts are of unusually high-pressure origin. However, in the absence of free C or other conventional indicators, this hypothesis remains untested. Although P substitution in silicate garnet has a considerable pressure dependence (Konzett and Frost 2009), experimental characterization of P in garnet in compositions more directly relevant to typical crustal garnet compositions has been limited.

This raises a larger problem regarding the identification of crustal UHP metamorphism, which remains largely dependent on the formation and preservation of coesite and/or diamond, especially in higher temperature settings. Although pseudosection modeling can predict peak assemblages—even for rocks low in SiO_2 or C—accurate results require knowledge of the bulk rock geochemistry during prograde to peak conditions, which is commonly unknown, particularly for rocks that fully recrystallized during exhumation. Garnet is certainly a common and relatively refractory phase in most settings and is known to accept substituents such as P, Ti, and Zr under HP/UHP conditions (Haggerty et al. 1994; Brunet et al. 2006; Dwarzski et al. 2006). A record of such substituents may be preserved either in compositional zonation or by the presence of precipitates representing these substituents originally in the garnet structure. Further experimental calibration of these substitutions in relevant compositions may allow for a more quantitative interpretation of the P-T histories of garnet of unusual minor-element composition and/or containing multiphase precipitate suites, thus expanding the indicators by which we might identify (U)HP metamorphism.

Metamorphic rims on zircon

Dissolution-reprecipitation involves dynamic, synchronous dissolution of zircon coupled with a simultaneous reprecipitation of zircon along a reaction front that propagates from the rim towards the core. The reaction front can produce compositional changes in minor and trace elements (Tomaschek et al. 2003; Geisler et al. 2007; Rubatto et al. 2008) and enable complete removal of radiogenic Pb, thereby resetting the age of the geochronometer. Previous studies also cite the presence of nm- to μm-scale pores in zircon as evidence of dissolution-reprecipitation (Geisler et al. 2007; Vonlanthen et al. 2012), but these pores may not be preserved due to metamorphism (Tomaschek et al. 2003).

Based on these criteria, we interpret that the metamorphic rims on zircon in both populations were formed primarily from inward propagation of dissolution-reprecipitation reaction fronts. Components from the original zircon—i.e. U, Y, P, and, notably, Th—are now concentrated at the leading edge of the reaction front in the CL-dark band, adjacent to the unreacted core. Much of the original U, Y, P, and all the original Th have been concentrated in this band of anomalous xenotime-rich zircon solid solution. These components are interpreted to represent mainly redistribution of xenotime component from zircon in response to metamorphism along a low-temperature/high-pressure path, as suggested by experimental work on zircon-xenotime solid solution by Tomaschek (2010). Alternative explanations for this distribution must call on a phase of deposition/growth (on the resorbed core) of a thin shell of new zircon with extremely elevated U, Th, Y, and P, followed by further growth of new zircon, which in zircon1 is entirely without Th (**Fig. 9**).

Although we do not know where the Pb from the dissolution-reprecipitation metasomatized rims collects, dissolution-reprecipitation can be effective at removing radiogenic Pb, effectively resetting the chronometer for the metasomatized rims. In some cases, dissolution-reprecipitation does not remove all the radiogenic Pb during (re)crystallization of the rims, as evident in **Fig. 7a**. Because of low concentrations of U in the convolute rims (ca. 20–50 ppm), minor trapped radiogenic Pb (and common-Pb) can significantly affect the analysis, making it apparently older than the inner rim. The inner rim, however, has much higher U concentrations (~900 ppm) making any small amount of inherited Pb much less significant.

Zircon1 has several unique geochemical signatures. First, the Th-rich band around unreacted zircon cores is a strong marker of the maximum extent of the inward propagation of the metasomatic front. The lack of measurable Th in zircon1 rims (**Fig. 9a-b; Table 1**) indicates: 1) complete exclusion of Th during the metasomatic process, and 2) an absence of Th from the source material for any new zircon growth that might have occurred. Second, zircon1 rims have a monotonic HfO_2 content that is unique to each garnet megacryst, but does not correspond to the composition of the zircon1 core or its position within the host garnet (**Fig. 9, Table 1**). The rim composition differs between RBTS- and WMBTS-hosted zircon. Zircon1 rims are homogeneous in Hf from the outer margin against the host garnet to the inner margin of the zircon rim against the unreacted core. Further, the zircon1 rim compositions are distinct from the zircon2 rims, even on grains located immediately adjacent to the megacrysts, such as Matrix1 from WMBTS (**Figs. 5b, 8c**). These data imply that with regard to Hf, the zircon1 rim composition was buffered throughout its formation and in a domain coextensive with the garnet host. Third, the steep HREE profile, lack of Ce anomaly, and overall lower concentration of HREE of the zircon1 rims is distinctive and anomalous. If zircon1 rims formed exclusively from dissolution-reprecipitation, the rim compositions should be consistent with the original core, which is not the case. If the rims formed in equilibrium with garnet under typical metamorphic conditions, the HREE profile of the zircon rim should be consistent with the HREE profile of the co-existing garnet (e.g. Rubatto 2002; Hoskin and Schaltegger 2003; Harley et al. 2007). A transect across the co-existing garnet megacryst via LA-ICPMS (see Data Supplement Figure 2, Table 3) yielded a flat HREE profile, which suggests that either zircon is not in equilibrium with this garnet or that the conditions that formed these rims favor REE partitioning between the reacting phases. An alternative explanation is the addition of components to form new zircon from a material relatively depleted in REE compared to zircon. The local volumetric increase, recorded by the distinctive radial fractures surrounding nearly all zircon1 grains, confirms some amount of growth (i.e. addition of new material). New material sourced externally to the garnet (e.g. a fluid) would require transport of at least Zr and Hf across many cm of intact garnet while maintaining *all* the geochemical characteristics described above. We therefore conclude that the contribution of new material and the fluid associated with the metasomatic reactions are both locally derived from the host garnet.

Hydrogen and Na can be minor substituents in garnet under HP/UHP conditions. Hydrogen enters the garnet structure as OH or H_4O_4 to at least 2500ppm (as H_2O) at UHP (Gong et al. 2013) whereas garnet typically contains only tens to hundreds of ppm at crustal pressure (Maldener et al. 2003). Similarly, significant Na enters the garnet structure at up to 0.22 wt% Na_2O at several GPa in mantle examples (Sobolev and Lavrent'ev 1971) yet elevated Na is found in crustal HP/UHP garnet only to a limited extent (e.g. Schertl et al. 1991). The disparity between the possible and the typically observed H and Na content in HP/UHP garnet may indicate that these substituents exited the garnet on decompression. We suggest that HP/UHP garnet that has incorporated significant H and Na may experience metasomatic effects during decompression from the release of endogenous alkali-bearing fluid when these substituents exit the garnet structure. Such an endogenous fluid may have participated in the reactions that produced the metamorphic rims in zircon1.

Growth of zircon within garnet requires mass transfer of zircon components, particularly Zr and Hf. Typical garnet at crustal pressure (<1GPa) contains tens of ppm Zr (e.g. Fraser et al. 1997, Degeling et al. 2001). However, experiments have shown that garnet can incorporate up to 6000 ppm Zr at pressures of 5 to 7 GPa (Dwarzski et al. 2006), indicating increased solubility of Zr (and presumably, Hf) in garnet under UHP conditions. The order of magnitude difference in Zr solubility in garnet between UHP and crustal conditions may provide a source for such mass transfer to have occurred between garnet and the included zircons, if such a pressure excursion occurred and diffusivity was sufficient.

The coarse rutile precipitates in the phosphatic garnet megacrysts also indicate a period of long-range diffusivity of another tetravalent cation (Ti) in octahedral coordination. Under typical crustal and UHT conditions, Ti in garnet substitutes for Si in tetrahedral coordination (Kawasaki and Motoyoshi 2007). However, at elevated pressure (>1GPa), Ti in garnet is almost entirely in octahedral coordination (Ackerson et al. 2013). Precipitation of coarse rutile blades and bicrystals in the phosphatic garnet megacrysts may have proceeded by open-system precipitation mechanisms as described by Proyer et al. (2013).

The composition of the myriad ca. 1 μm zircon crystals in the phosphatic garnet megacrysts is unknown due to analytical limitations for very small volumes, but their broad distribution and relatively uniform size and morphology suggest precipitation from an originally higher-Zr host garnet. If so, the addition of new material to the metamorphic rims of the included detrital zircon would be merely another aspect of the process of zircon precipitation from the bulk garnet. If not, the micro-zircons are matrix inclusions and each phosphatic garnet overgrew a pre-existing distribution of micro-zircons. However, this would require a pre-existing concentration of micro-zircons on the order of $10^8/cm^3$ over volumes on the order of 10s of cm^3, with evidence for this distribution having been preserved only within the phosphatic garnet megacrysts.

To summarize, the rims on zircon1 show evidence of two metamorphic mechanisms. First, dissolution-reprecipitation reactions are indicated by the CL-dark reaction front enriched in Th, U, Y, and P adjacent to the unreacted core. Second, the extensive fracturing of the surrounding garnet host indicates local volumetric increase of zircon (i.e. growth). No unusual fracturing is observed around any other inclusions in garnet. Because simple mixing between zircon and garnet does not entirely explain the anomalous chemistry of the zircon1 rims, we interpret that these rim compositions were produced by both metamorphic mechanisms: dissolution-reprecipitation reaction that removed and relocated xenotime component (and potentially HREE?) from the rims and of the addition of components from garnet. The uniform composition of the metamorphic rims (**Fig. 7**) indicates that both metamorphic processes were operating simultaneously.

In zircon2, the accumulation of U, Y, P, and Th at the core-rim boundary provides clear evidence of dissolution-reprecipitation reactions similar to those in the megacrysts, but there is no certain evidence of growth. The metamorphic rims have generally higher Hf (**Fig. 9**) and much lower Th/U (**Fig. 11b**) than the cores, but they lack the distinctive signatures of fixed Hf and no measurable Th. Some rims are consistent with equilibration with garnet, whereas others suggest equilibration with a metamorphic fluid. These data indicate that the rim compositions are controlled by local changes in mineralogy and the presence and availability of fluids and melt over 30 million years of metamorphism.

Chronology of events

The oscillatory CL zoning and compositions of zircon cores from both populations indicate a magmatic or volcanogenic source of detrital grains that were subsequently metamorphosed. In zircon1, the cores are dominantly Paleozoic and range from 447 to 404 Ma (n = 28). The population lacks Grenville dates, which typically dominate the detrital zircon signature in lithologies from this region (e.g. Cawood and Nemchin 2001; Murphy et al. 2004; van Staal et al. 2009). In contrast, zircon2 cores yield a broad range of concordant dates. Proterozoic dates are common and range from 1726 to 562 Ma (**Fig. 11; Table 2**). Paleozoic dates range from 533 to 415 Ma (n = 17), most of which cluster near 475 Ma. The older dates are broadly consistent with the signature of the Laurentian margin (see Data Supplement Figure 3), but may also include contributions from other terranes—the sample size is too small to fully address provenance. The Paleozoic dates in both populations are interpreted as zircon shed from nearby magmatic arcs during the Taconic through early Acadian (475 to 404 Ma). The youngest concordant zircon core date pins deposition to 404 Ma.

The timing of the reaction producing the CL-dark boundary between the core and rim cannot be dated directly. However, the metamorphic rims beyond the band are commonly large enough to analyze via LASS and geochemistry is essential in deciphering the metamorphic mechanism(s) that produced the zircon rims. The HREE profiles at the oldest zircon1 locations (400 and 396 Ma) are significantly steeper than the younger concordant zircon1 (385 to 373 Ma). These data suggest that the unique conditions and reactions (endogenous fluids and growth from garnet) that formed the zircon1 rims with the steepest HREE profiles were perhaps short in duration (400 to 396 Ma) and that the analyses with more typical REE profiles signal a return to granulite to amphibolite facies metamorphism by 395 Ma. The youngest dates (377 and 373

Ma) are geochemically consistent with igneous growth, suggesting the presence of melt during this interval.

The composition of zircon2 rims also support granulite to amphibolite facies conditions by 395 Ma. Half of the REE profiles are similar to zircon2 cores and lack the steep HREE profiles observed in some of zircon1 rims. The other REE profiles from zircon2 rims indicate garnet stability. The long duration of metamorphism (394 to 365 Ma) and varied compositions (**Fig. 10a**) are consistent with zircon response to local changes in mineralogy and fluid/melt composition and/or availability over this interval, which generally agrees with regional constraints for the timing of the high-temperature Acadian orogeny (e.g. Pyle and Spear 2002; Cheney et al. 2006, Gatewood et al. 2015). The fluid that catalyzed the production of metamorphic rims on zircon2 may have been sourced from a variety of reactions associated with the high-temperature Acadian, including the melt-producing reactions that ultimately produced the restitic schist.

The restitic nature of the schist requires that melt was extracted, but the effect of melting on garnet and zircon varies among these samples. The pristine, intact megacryst in WMBTS indicates that some garnet megacrysts persisted through melting without modification, but resorption of the garnet megacrysts in RBTS and the presence of epidote along fractures within these megacrysts indicate a response to the presence of fluid and/or melt. The oldest dates and the steepest HREE profiles of metamorphic zircon are included within the pristine megacryst and suggest net growth of zircon, not net dissolution. The younger metamorphic rim dates in both zircon1 and zircon2 are consistent with either modification of zircon via metasomatic dissolution-reprecipitation or some component of igneous growth after 395 Ma. Some new growth of metamorphic zircon may have occurred in zircon2, but it can only be confirmed in zircon1 where the presence of radial fractures of the host garnet indicates net growth of zircon. Although many of the zircon2 rims were likely produced from metasomatic fluids associated with melting, the precise timing of melt production cannot be directly determined from the zircon data.

IMPLICATIONS

Metamorphic growth and modification of zircon

Recent Zr budget studies demonstrate the limited capacity for crystallization of new zircon (i.e. overgrowths) within common metamorphic systems (Degeling et al. 2001; Kohn et al. 2015). Yet, concordant rims on zircon recording metamorphic events are common in polymetamorphic systems. Metasomatism by dissolution-reprecipitation has emerged as an alternative to overgrowth as a mechanism for producing datable metamorphic rims on zircon (Tomaschek et al. 2003; Geisler et al. 2007). Zircon1 and zircon2 yield abundant evidence of dissolution-reprecipitation mechanisms in the formation of metamorphic zircon rims. However, the radial fractures around zircon1 also indicate volumetric expansion (new growth), and thus an unusual setting where both processes have been confirmed.

Many examples of dissolution-reprecipitation mechanisms in zircon exhibit the lobate boundary between core and rims (e.g. Vonlanthen et al. 2012). In addition to these features, the zircons in this study also have a thin CL-dark band found at the core-rim boundary. The CL-dark band is tied to trace-element accumulations at the reaction front and has not been observed in other zircon studies, with the exception of the diamondiferous UHP locality near Xanthi, in the Central Rhodope, Greece (cf. Fig. 11e; Krenn et al. 2010). One of the most distinctive features of the trace-element accumulation at the edge of the unreacted core is the sharp accumulation of Th and U. Thorium is much more spatially restricted than U and appears to be excluded from the rest of the rim. These observations are similar to laboratory experiments with dissolution-reprecipitation reactions in xenotime, where Harlov and Wirth (2012) observed an accumulation of Th along the reaction front and an exclusion from the rest of the rim domain. Quantification of the Th accumulation (hence the quantity of reacted zircon, if its original Th content is known) and evaluation of the Th budget in the metamorphic rim may allow for evaluation of the relative contribution of dissolution-reprecipitation and growth processes in metamorphic zircon.

These data prompt questions about the fidelity of metamorphic zircon. What do these dates mean? Do they record metamorphic events? The data demonstrate that most rim analyses are concordant, which suggests that the dates can be related to the timing of metasomatism. The composition also provides insight regarding the conditions of metasomatism. For example, the rim dates from zircon2 suggest that zircon grew in equilibrium with garnet for portions of the metamorphic history and in equilibrium with non-garnet stable fluids for other portions.

Collectively, these data indicate that the matrix phase assemblage was changing over the 30 Myr interval. The relatively small number of rim analyses (19) compared with core (119) suggests that more detailed information regarding the metamorphic evolution of the phase assemblage would require measuring a more reactive phase where larger portions of the mineral retain information about metamorphism. Monazite is an excellent chronometer to address these questions—particularly the timing of melt-generation—but the lack of monazite within the pristine megacrysts suggests that a record derived solely from monazite will be incomplete. Because zircon is present in all petrographic contexts, it remains an useful target for constructing the entire metamorphic history, though perhaps at broader strokes.

Rims with high common-Pb and/or discordance suggest that the conditions responsible for forming metamorphic zircon can be complex. The presence of high common Pb may be related to the composition of the metasomatic fluid, the P-T conditions of metasomatism, or the potential contributions of constituents from other phases (e.g. phosphatic garnet) to grow new zircon. We do not have enough data to resolve among these possibilities, but detailed atomic scale analysis of the reaction boundary itself (e.g. APT analysis) may provide insight regarding the distribution and possible source of common-Pb. Discordant analyses may reflect the incomplete removal of radiogenic Pb from this original zircon or mixing of different domains (e.g. core and rim), but this falls beyond the resolution of the techniques employed in this study. Further improvements in spatial resolution will permit analysis of thin domains and will likely resolve some of the ambiguities presented here.

Regional implications

The near absence of older zircon cores within the garnet megacrysts, as compared to the adjacent matrix, presents an interesting problem. One explanation is that the phosphatic garnet megacrysts grew in a tightly restricted setting in a protolith that did not contain the same Proterozoic component of zircon present in their matrix. An alternative explanation is that the garnet preferentially resorbed Proterozoic zircon during growth because they had accumulated more radiation damage and were therefore more labile than other zircon grains in the detrital population. In this case, the zircon clusters found in some garnet specimens (**Fig. 3d**) represent locally high concentrations of zircon components within the garnet and may reflect resorbed detrital zircon.

The LASS dates on zircon cores and rims indicate that the original deposition concluded by ca. 404 Ma and that metamorphism began shortly thereafter—by c. 400 Ma. The timing and geochemistry of these analyses suggest three important things. First, the detrital zircon cores record an approaching island arc (or arcs) proximal to Laurentia active ca. 447 to 404 Ma. Second, zircon1 rims record some of the earliest metamorphism (ca. 400 Ma) associated with the conventional Acadian may have been at HP/UHP conditions. Third, these grains record continued metamorphism from 395 Ma until the end of the Acadian (ca. 365 Ma), suggesting that these rocks record nearly the entire history of Acadian metamorphism in the region.

ACKNOWLEDGEMENTS

This research was partially supported by NSF EAR 0948158 and Bowdoin College Research Funds. The Ultrachron development project was supported by NSF EAR-0004077 and NSF EAR-0549639 to M.L. Williams and M.J. Jercinovic at the University of Massachusetts, and collaboratively by Cameca. We thank Seth Kruckenberg (Boston College) and Gareth Seward (UCSB) for assistance with CL imaging. We thank Jane Gilotti for editorial handling of the manuscript and Daniel Harlov and Ethan Baxter for providing helpful comments on a previous draft of this manuscript.

REFERENCES CITED

Ackerson, M.R., Tailby, N., Watson, E.B., and Spear, F.S. (2013) Variations in Ti coordination and concentration in garnet in response to temperature, pressure and composition. Abstract. 2013 Fall Meeting, San Francisco, California.

Allaz, J., Williams, M.L., Jercinovic, M.J., and Donovan, J. (2011) A new technique for electron microprobe trace element analysis: The multipoint background method. EMAS 2011, Book of Tutorials and Abstracts: Modern Developments and Applications in Microbeam Analysis, May 2011, Angers, France. 319–320.

Armstrong, T.R., Tracy, R.J., and Hames, W.E. (1992) Contrasting styles of Taconian, Eastern Acadian and Western Acadian metamorphism, central and western New England. Journal of Metamorphic Geology, 10, 415-426. DOI: 10.1111/j.1525-1314.1992.tb00093.x

Axler, J.A., and Ague, J.J. (2015) Exsolution of rutile or apatite precipitates surrounding ruptured inclusions in garnet from UHT and UHP rocks: Journal of Metamorphic Geology, v. 33, 829-848. doi:10.1111/jmg.12145

Brunet, F., Bonneau, V., and Irifune, T. (2006) Complete solid-solution between $Na_3Al_2(PO_4)_3$ and $Mg_3Al_2(SiO_4)_3$ garnets at high pressure. American Mineralogist, 91, 211-215. doi:10.2138/am.2006.2053

Cawood, P.A. and Nemchin, A.A. (2001) Paleogeographic development of the east Laurentian margin: Constraints from U-Pb dating of detrital zircons in the Newfoundland Appalachians. GSA Bulletin, 113, 9, 1234-1246. doi: 10.1130/0016-7606(2001)113<1234:PDOTEL>2.0.CO;2

Cheney, J.T., Spear, F.S., and Kirk-Lawlor, N., (2006) The mysterious machinations of muscovite and monazite during metamorphism or How the CVS (Connecticut Valley synclinorium) survived PMS (post-metamorphic-stretching): Geological Society of America Abstracts with Programs, v. 38, p. 49. https://gsa.confex.com/gsa/2006AM/finalprogram/abstract_113956.htm

Cherniak, D.J. and Watson, E.B. (2001) Pb diffusion in zircon. Chemical Geology, 172, 1, 5-24. http://dx.doi.org/10.1016/S0009-2541(00)00233-3

Cherniak, D. J., Watson, E. B., Grove, M., and Harrison, T. M. (2004) Pb diffusion in monazite: A combined RBS/SIMS study. Geochimica et Cosmochimica Acta, 68, 829-840. doi:10.1016/j.gca.2003.07.012

Corfu, F., Hanchar, J.M., Hoskin, P.O.W. and Kinny, P. (2003) Atlas of zircon textures. Reviews in Mineralogy and Geochemistry, v. 53, no. 1, p. 469–500.

Degeling, H., Eggins, S., and Ellis, D.J. (2001) Zr budgets for metamorphic reactions, and the formation of zircon from garnet breakdown. Mineralogical Magazine, 65, 749–758. doi:10.1180/002646101316560006

Dwarzski, R.E., Draper, D.S., Shearer, C.K., and Agee, C.B. (2006) Experimental insights on crystal chemistry of high-Ti garnets from garnet-melt partitioning of rare-earth and high-field-strength elements. American Mineralogist, 91, 1536-1546. doi:10.2138/am.2006.2100.

Fraser, G., Ellis, D., and Eggins, S. (1997) Zirconium abundance in granulite-facies minerals, with implications for zircon geochronology in high-grade rocks. Geology, 25, 7, 607-610. doi: 10.1130/0091-7613(1997)025<0607:ZAIGFM>2.3.CO;2

Gatewood, M.P., Dragovic, B., Stowell, H.H., Baxter, E.F., Hirsch, D.M., and Bloom, R. (2015) Evaluating chemical equilibration in metamorphic rocks using major element and Sm-Nd isotopic age zoning in garnet, Townshend Dam, Vermont, USA. Chemical Geology, 401, 151-168. http://dx.doi.org/10.1016/j.chemgeo.2015.02.017

Geisler, T., Schaltegger, U., and Tomaschek, F. (2007) Re-equilibration of Zircon in Aqueous Fluids and Melts. Elements, 3, 43-50. doi:10.2113/gselements.3.1.43

Gong, B., Chen, R-X., and Zheng, Y-F. (2013) Water contents and hydrogen isotopes in nominally anhydrous minerals from UHP metamorphic rocks in the Dabie-Sulu orogenic belt, Chinese Science Bulletin, 58, 35, 4384-4389. DOI: 10.1007/s11434-013-6069-7

Haggerty, S.E., Fung, A.T. and Burt, D.M. (1994). Apatite, phosphorus and titanium in eclogitic garnet from the upper mantle. Geophysical Research Letters 21, 16, 1699-1702. doi: 10.1029/94GL01001. issn: 0094-8276.

Harley, S.L., Kelly, N.M., and Möller, A. (2007) Zircon behavior and the thermal histories of mountain chains. Elements, 3, 25-30. doi:10.2113/gselements.3.1.25

Harlov, D.E., Wirth, R., and Hetherington, C.J. (2011) Fluid-mediated partial alteration in monazite: the role of coupled dissolution-reprecipitation in element redistribution and mass transfer. Contributions to Mineralogy and Petrology, 162, 329-348. DOI: 10.1007/s00410-010-0599-7.

Harlov, D.E., Lewerentz, A., and Schersten, A. (2012) Alteration of zircon in alkaline fluids: Nature and Experiment. Mineralogical Magazine, 76, 6, 1813. http://goldschmidtabstracts.info/2012/1813.pdf

Hay, D.C. and Dempster, T.J. (2009) Zircon Behaviour during Low-temperature Metamorphism. Journal of Petrology, 50, 4, 571-589. doi:10.1093/petrology/egp011

Hatch, N.L., Jr. and Warren, C.R. (1981) Geologic map of the Goshen quadrangle, Franklin and Hampshire Counties, Massachusetts. U.S. Geological Survey Geologic Quadrangle Map GQ-1561, scale 1: 24,000. http://pubs.er.usgs.gov/publication/gq1561

Hoskin, P.W.O., and Schaltegger, U. (2003) The Composition of Zircon and Igneous and Metamorphic Petrogenesis: Reviews in Mineralogy and Geochemistry, v. 53, no. 1, p. 27-62.

Jackson, S.E., Pearson, N.J., Griffin, W.L., and Belousova, E.A., (2004) The application of laser ablation-inductively coupled plasma-mass spectrometry to in situ U/Pb zircon geochronology: Chemical Geology, v. 211, no. 1–2, p. 47–69.

Karabinos, P., Samson, S.D., Hepburn, J.C., and Stoll, H.M. (1998) Taconian Orogeny in the New England Appalachians; collision between Laurentia and the Shelburne Falls Arc. Geology, 26, 215-218. doi: 10.1130/0091-7613(1998)026<0215:TOITNE>2.3.CO;2

Kawasaki, T., and Motoyoshi, Y. (2007) Solubility of TiO2 in garnet and orthopyroxene: Ti thermometer for ultrahigh-temperature granulites. U.S. Geological Survey and The National Academies; USGS OF-2007-1047, Short Research Paper 038; http:// dx.doi.org/10.3133/of2007-1047.srp038.

Kohn, M.J., Corrie, S.L., and Markley, C. (2015) The rise and fall of metamorphic zircon. American Mineralogist, 100, 897-908. doi: 10.2138/am-2015-5064

Konzett, J. and Frost, D.J. (2009) The high P-T stability of hydroxyl-apatite in natural and simplified MORB-an experimental study to 15 GPa with implications for transport and storage of phosphorus and halogens in subduction zones. Journal of Petrology, 50, 2043–2062. doi: 10.1093/petrology/egp068

Krenn, K., Bauer, C., Proyer, A., Klötzli, U., and Hoinkes, G. (2010) Tectonometamorphic evolution of the Rhodope orogen. Tectonics, 29, TC4001, doi:10.1029/2009TC002513.

Kusiak, M.A., Whitehouse, M.J., Wilde, S.A., Nemchin, A.A., and Clark, C. (2013) Mobilization of radiogenic Pb in zircon revealed by ion imaging: Implications for early Earth geochronology. Geology, 41, 291-294. doi:10.1130/G33920.1

Kylander-Clark, A.R.C., Hacker, B.R., and Cottle, J.M. (2013) Laser-ablation split-stream ICP petrochronology. Chemical Geology. 345, 99-112. dx.doi.org/10.1016/j.chemgeo.2013.02.019

Macdonald, F.A., Ryan-Davis, J., Coish, R.A., Crowley, J.L., and Karabinos, P. (2014) A newly identified Gondwanan terrane in the northern Appalachian Mountains: Implications for the Taconic orogeny and closure of the Iapetus Ocean. Geology, 30, 1095-1098. doi:10.1130/G35659.1

Maldener, J., Hösch, A., Langer, K., and Rauch, F. (2003) Hydrogen in some natural garnets studied by nuclear reaction analysis and vibrational spectroscopy. Physics and Chemistry of Minerals, 30, 6, 337-344. DOI: 10.1007/s00269-003-0321-7

Murphy, J.B., Fernandez-Suarez, J., Keppie, J.D., and Jeffries, T.E. (2004) Contiguous rather than discrete Paleozoic histories for the Avalon and Meguma terranes based on detrital zircon data. Geology, 32, 7, 585-588. doi: 10.1130/G20351.1

Mposkos, E.D. and Kostopoulis, D.K. (2001) Diamond, former coesite and supersilicic garnet inmetasedimentary rocks from the Greek Rhodope: a new ultrahigh-pressure metamorphic province established. Earth and Planetary Science Letters, 192, 497-506. doi:10.1016/S0012-821X(01)00478-2

O'Brien, T.M. and Koziol, A.M. (2008) Thermobarometry in Kyanite S-tectonite gneisses from the Goshen Dome, Connecticut Valley Zone, western Massachusetts. Geological Society of America Abstracts with Programs, 40, 1, 20. https://gsa.confex.com/gsa/2008NE/finalprogram/abstract_134851.htm

Paton, C., Woodhead, J., Hellstrom, J., Hergt, J., Greig, A., and Maas, R. (2010) Improved laser ablation U-Pb zircon geochronology through robust downhole fractionation correction, Geochemistry Geophysics Geosystems, 11, 36 p., doi:10.1029/2009GC002618.

Proyer, A., Habler, G., Abart, R., Wirth, R., Krenn, K., and Hoinkes, G. (2013) TiO_2 exsolution from garnet by open-system precipitation: evidence from crystallographic and shape preferred orientation of rutile inclusions. Contributions to Mineralogy and Petrology, 166, 211-234. doi: 10.1007/s00410-013-0872-7.

Pyle, J.M. and Spear, F.S. (2003) Four generations of accessory-phase growth in low-pressure migmatites from SW New Hampshire. American Mineralogist, 88, 338-351. doi:10.2138/am-2003-2-311.

Pyle, J.M., Spear, F.S., Cheney, J.T., and Layne, G. (2005) Monazite ages in the Chesham Pond Nappe, SW New Hampshire, U.S.A.: Implications for assembly of central New England thrust sheets. American Mineralogist, 90, 592-606. doi:10.2138/am.2005.1341

Robinson, P., Tucker, R.D., Bradley, D., Berry, H.N. IV, and Osberg, P.H. (1998) Paleozoic orogens in New England, USA. GFF, 120, 119–148. https://pubs.er.usgs.gov/publication/70020369

Rubatto, D. (2002) Zircon trace element geochemistry: partitioning with garnet and the link between U–Pb ages and metamorphism. Chemical Geology, 184, 1, 123-138. doi:10.1016/S0009-2541(01)00355-2

Rubatto, D., Muntener, O., Barnhoorn, A., and Gregory, C. (2008) Dissolution-reprecipitation of zircon at low-temperature, high-pressure conditions (Lanzo Massif, Italy). American Mineralogist, 93, 10, 1519-1529. doi: 10.2138/am.2008.2874

Ruiz Cruz, M.D. and Sanz de Galdeano, C. (2013) Coesite and diamond inclusions, exsolution microstructures and chemical patterns in ultrahigh pressure garnet from Ceuta (Northern Rif, Spain). Lithos, 177, 184–206. doi:10.1016/j.lithos.2013.06.004

Russell, A. (2012) Oxygen isotopes in garnet from eclogite: Oxygen isotope geochemistry of the Bohemian Massif and zoning revealed by secondary ion mass spectrometry. Master's Thesis, University of Wisconsin, 291p. http://search.library.wisc.edu/catalog/ocn794415471

Schertl, H.-P., Schreyer, W., Chopin, C. (1991) The pyrope-coesite rocks and their country rocks at Parigi, Dora Maira Massif, Western Alps: Detailed petrography, mineral chemistry and PT-path. Contributions to Mineralogy and Petrology, 108, 1-21. DOI: 10.1007/BF00307322

Schwartz, J.J., John, B.E., Cheadle, M.J., Wooden, J.L., Mazdab, F., Swapp, S., and Grimes, C.B. (2010) Dissolution–reprecipitation of igneous zircon in mid-ocean ridge gabbro, Atlantis Bank, Southwest Indian Ridge. Chemical Geology, 274, 68-81. doi:10.1016/j.chemgeo.2010.03.017

Slama, J., Košler, J., Condon, D.J., Crowley, J.L., Gerdes, A., Hanchar, J.M., Horstwood, M.A., Morris, G.A., Nasdala, L., Norberg, N., Schaltegger, U., Schoene, B., Tubrett, M.N., and Whitehouse, M.J. (2008) Plešovice zircon; a new natural reference material for U/Pb and Hf isotopic microanalysis: Chemical Geology, v. 249, no. 1–2, p. 1–35.

Snoeyenbos, D.R., Koziol, A., Russell, A., Ebel, D.S., and Valley, J.W. (2011) Prograde Growth History of Possible Relic UHP Garnets from the Taconian of Western Massachusetts. American Geophysical Union, Fall Meeting 2011, abstract #V21G-04.

Snoeyenbos, D.R., Reinhard, D. and Olson, D., (2012) Atomic Scale Imaging of U, Th and Radiogenic Pb in Zircon. Goldschmidt Conference 2012. http://goldschmidtabstracts.info/2012/2388.pdf

Snoeyenbos, D.R., Peterman, E., Jercinovic, M., Williams, M., and Reinhard, D. (2013) Isotopic Tomography of Monazite. *Mineralogical Magazine*, 77, 5, 2231. http://goldschmidt.info/2013/abstracts/finalPDFs/2231.pdf

Sobolev, N.V., Jr. and Lavrent'ev, J. G. (1971) Isomorphic Sodium Admixture in Garnets Formed at High Pressures. Contributions to Mineralogy and Petrology, v. 31, p. 1-12. doi:10.1007/BF00373387

Terry, M.P. and Robinson, P. (2004) Geometry of eclogite-facies structural features: Implications for production and exhumation of ultrahigh-pressure and high-pressure rocks, Western Gneiss Region, Norway. Tectonics, 23, TC2001. doi: 10.1029/2002TC001401

Tomaschek, F., Kennedy, A.K., Villa, I.A., Lagos, M., and Ballhaus, C. (2003) Zircons from Syros, Cyclades, Greece—Recrystallization and mobilization of zircon during high-pressure metamorphism. Journal of Petrology, 44, 11, 1977-2002. doi: 10.1093/petrology/egg067

Valley, J.W., Reinhard, D.A., Cavosie, A.J., Ushikubo, T., Lawrence, D.F., Larson, D.J., Kelly, T.F., Snoeyenbos, D.R., and Strickland, A. (2015) Nano- and micro-geochronology in Hadean and Archean zircons by atom-probe tomography and SIMS: New tools for old minerals. American Mineralogist, 100, 1355-1377. http://doi.org/10.2138/am-2015-5134

van Roermund, H., Drury, M., Barnhoorn, A., and de Ronde, A. (1999) Garnet microstructures from an ultra-deep (>185km) orogenic peridotite. Ofioliti, 24, 185-186. doi: 10.4454/ofioliti.v24i1b.94

van Staal, C.R., Whalen, J.B., Valverde-Vaquero, P., Zagorevski, A., and Rogers, N. (2009) Pre-Carboniferous, episodic accretion-related, orogenesis along the Laurentian margin of the northern Appalachians. In Ancient Orogens and Modern Analogues. Edited by J.B. Murphy, J.D. Keppie, and A.J. Hynes. Geological Society of London Special Publication *327*, 271–316. doi: 10.1144/SP327.13.

Vonlanthen, P., Fitz Gerald, J.D., Rubatto, D., and Hermann, J. (2012) Recrystallization rims in zircon (Valle d'Arbedo, Switzerland): An integrated cathodoluminescence, LA-ICP-MS, SHRIMP, and TEM study. American Mineralogist, 97, 369-377. doi: 10.2138/am.2012.3854

Wiedenbeck, M., Allé, P., Corfu, F., Griffin, W.L., Meier, M., Oberli, F., von Quadt, A., Roddick, J.C. and Spiegel, W. (1995) Three natural zircon standards for U–Th–Pb, Lu–Hf, trace element and REE analyses: Geostandards Newsletter, v. 19, no. 1, p. 1–23.

Williams, M.L., Jercinovic, M.J., Harlov, D.E., Budzyn, B., and Hetherington, C.J. (2011) Resetting monazite ages during fluid-related alteration. Chemical Geology, 283, 218-225. doi:10.1016/j.chemgeo.2011.01.019

Ye, K., Cong, B. and Ye, D. (2000) The possible subduction of continental material to depths greater than 200 km. Nature, 407, 734-736. doi:10.1038/35037566

Figure Captions

FIGURE 1: Geologic maps of study area. **a)** Regional map showing geologic context of the Goshen Dome; adapted from Karabinos et al. (1998). **b)** The Goshen Dome, cored by the Collinsville Gneiss. The Cobble Mountain Formation contains restitic garnet-kyanite schist near the western margin, located within domains previously mapped as granulite and amphibolite gneisses. Yellow dots mark sample locations. Map modified from Hatch and Warren (1981).

FIGURE 2: RBTS. **a)** Plane polarized light photomicrograph. X-ray composition maps of **b)** Ca Kα and **c)** Mn Kα. Red dots mark locations of analyzed zircons; red arrow marks the location of the **d)** quantitative profile showing Mg# ($X_{Prp}/(X_{Prp} + X_{Alm})$), X_{Sps}, X_{Grs}, and wt% P_2O_5 versus distance across the garnet in μm.

FIGURE 3: RBTS. **a)** Plane polarized light photomicrograph of zircon inclusion wholly contained within garnet, showing radial fractures. Sub-μm apatite precipitates and oriented rutile needles cloud the host garnet. **b)** Backscattered electron (BSE) image of a zircon inclusion within garnet with radial fractures and abundant μm-scale zircon crystals (bright flecks) in the host garnet. **c)** Plane polarized light photomicrograph of rutile precipitates; many are twinned. **d)** BSE image of zircon needles and blades in garnet.

(DOI will not work until issue is live.) DOI: http://dx.doi.org/10.2138/am-2016-5524

FIGURE 4: a) Compositional profile near-core to rim of garnet RBTS-B (adjacent to garnet RBTS) shows Mg# ($X_{Prp}/(X_{Prp} + X_{Alm})$), X_{Sps}, X_{Grs}, and wt% P_2O_5. Sub-μm hydroxylapatite inclusions are abundant to the left of the red dashed line (near the core) and conspicuously absent to the right of the line (towards the rim), where intrinsic wt% P_2O_5 increases and XGrs drops to ca. 0.03. **b)** Plane polarized light photomicrograph showing location of compositional profile. Intrinsic P_2O_5 is anticorrelated to the presence of apatite inclusion trails.

FIGURE 5: WMBTS. **a)** Plane polarized light photomicrograph. X-ray composition maps of **b)** Ca Kα and **c)** Mn Kα. Red dots mark locations of analyzed zircon1; two matrix zircons are indicated in yellow. Red arrow marks the location of the **d)** quantitative profile showing Mg# ($X_{Prp}/(X_{Prp} + X_{Alm})$), X_{Sps}, X_{Grs}, and wt% P_2O_5.

FIGURE 6: G12B10. X-ray composition maps of **a)** Al Kα and **b)** Ca Kα. Red dots mark locations of analyzed zircon. **c)** Cross-polarized light photomicrograph. **d)** Plane-polarized light photomicrograph; mineral abbreviations: qtz = quartz, grt = garnet, chl = chlorite, pl = plagioclase, bt = biotite, crd = cordierite, ky = kyanite. Darkest minerals are rutile and ilmenite. All images are the same scale.

FIGURE 7: Representative zircon1 grains. **a)** From RBTS: cathodoluminescence (CL), laser ablation split stream (LASS) spot locations and corresponding ^{207}Pb-corrected $^{206}Pb/^{238}U$ dates, Hf Mα, and U Mβ maps. **b)** From WMBTS: CL, LASS spot locations and corresponding ^{207}Pb-

corrected $^{206}Pb/^{238}U$ dates, Hf Mα, Th Mα, U Mβ, and Y Lα maps; red arrows point to CL-dark, Th, U, Y, P enriched band at the margin of the unreacted core. **c)** From WMBTS: CL and Hf Mα map. U Mβ maps are not corrected for (minor) Th Mγ overlap due to much lower Th concentration and restricted spatial distribution Th vs. U. Note the characteristic CL-dark band between the unreacted core and the metamorphic rim and the homogeneity in Hf on the rims. Italicized dates are discordant; black LASS spots have high common-Pb.

FIGURE 8: Matrix zircon from G12B, G12G, and WMBTS. **a)** Cathodoluminescence (CL) and X-ray composition maps (Hf Mα, Th Mα, U Mβ, Y Lα, and P Kα) of a characteristic zircon found within kyanite in the matrix of G12B10; 20-µm scale on all images in this row. Hafnium is homogeneous in the rim and distinct from the core composition. The boundary between unreacted core and metamorphic rim is marked by a CL-dark band enriched in Th, U, Y and P. **b)** CL images of zircon grains from the matrix of G12B10 and G12G3. Circles mark laser ablation split stream (LASS) analysis spots with corresponding ^{207}Pb-corrected $^{206}Pb/^{238}U$ dates. Magmatic core domains labeled. Red arrows point to CL-dark, Th, U, Y, P enriched band at the margin of the unreacted core. Grains 12 and 30 are within chlorite; grain 48 is within rutile. **(c)** Matrix grain 1 from WMBTS (see **Fig. 5** for location) shown in CL and backscattered electron (BSE). Red boxes mark the location of WDS-EPMA maps (Hf Mα, Th Mα, U Mβ, and Y Lα). Note that the CL-dark band between the unreacted core and the metamorphic rims is also enriched in Hf, Th, U, and Y. Two bands of U and Y are also evident; see text for details.

FIGURE 9: Zircon included in garnet megacrysts in **a)** RBTS (n = 13 grains). **b)** WMBTS (n = 13 grains). **(c)** Matrix (n = 14 grains). Vertical gray lines separate analyses from different grains. Color-filled symbols are zircon core domains (typically 2 analyses per grain). The adjacent white-filled symbols (typically 2 analyses per grain) are the rim compositions directly next to the core. Dashed lines show the mean of core compositions; solid lines show the mean of rim compositions. Colored shading represents 1σ of the mean.

FIGURE 10: **A.** Rare earth element profiles from zircon1. Dashed lines are analyses with high common-Pb. Gray field marks a range of magmatic zircon compositions from igneous sources. **B.** Th/U vs. ^{207}Pb-corrected ^{206}Pb-^{238}U dates of zircon1; dates reflect 2σ uncertainty.

FIGURE 11: **A.** Rare earth element profiles from zircon2. The gray shaded region marks a range of magmatic zircon compositions from igneous rocks. **B.** Th/U vs. ^{207}Pb-corrected ^{206}Pb-^{238}U dates from zircon2; dates reflect 2σ uncertainty.

(DOI will not work until issue is live.) DOI: http://dx.doi.org/10.2138/am-2016-5524

Data Supplement Text

Figure 1: Cathodoluminescence (CL) images of zircon analyzed in this study. Circles mark the location of spot analyses and colored numbers are the ^{207}Pb corrected ^{206}Pb/^{238}U dates (in Ma). The grain number for each sample is shown in white.

Figure 2: Locations of garnet transects for geochemical analysis via laser ablation. The transect start is marked with a red circle; the end is marked with a red square.

Figure 3: Kernel density estimation of ^{207}Pb-corrected ^{206}Pb/^{238}U dates from zircon cores. Circles below the x-axis are the dates. Mixed spot analyses were excluded.

Data Tables

1: Electron microprobe analyses of zircon. Data were collected at UMass-Amherst.

2: Zircon geochronology and geochemistry analyses. Full analytical results. Data were collected at UC Santa Barbara.

3: Transects across garnet analyzed via laser ablation analysis. Full analytical results. Data were collected at UC Santa Barbara.

Table 1: Electron probe micro-analysis results from cores and rims in both zircon populations.

	n	**HfO_2**	**1σ**	**ThO_2**	**1σ**
RBTS – core	26	1.19	0.16	0.032	0.023
RBTS – rim	26	1.62	0.07	0.002	0.004
WMBTS – core	26	1.23	0.19	0.070	0.046
WMBTS – rim	25	1.54	0.05	0.003	0.006
Matrix – core	29	1.22	0.16	–	–
Matrix – rim	30	1.41	0.11	–	–

n = number of analyses

Detection limits at 99% confidence level: 0.016 wt% HfO_2 and 0.003 wt% ThO_2 for RBTS and WMBTS core and rim measurements. Analysis on SX-100 with multi-point backgrounds (Allaz et al., 2011; Probe for EPMA, Probe Software Inc.). HfO_2 matrix zircon analyses by SX-50 at lower precision, which is sufficient to confirm heterogeneity apparent from X-ray composition maps.

Table 2: U-Pb and rare earth element data of concordant ages from all samples, classified by core, overgrowth and sample (Excel document).

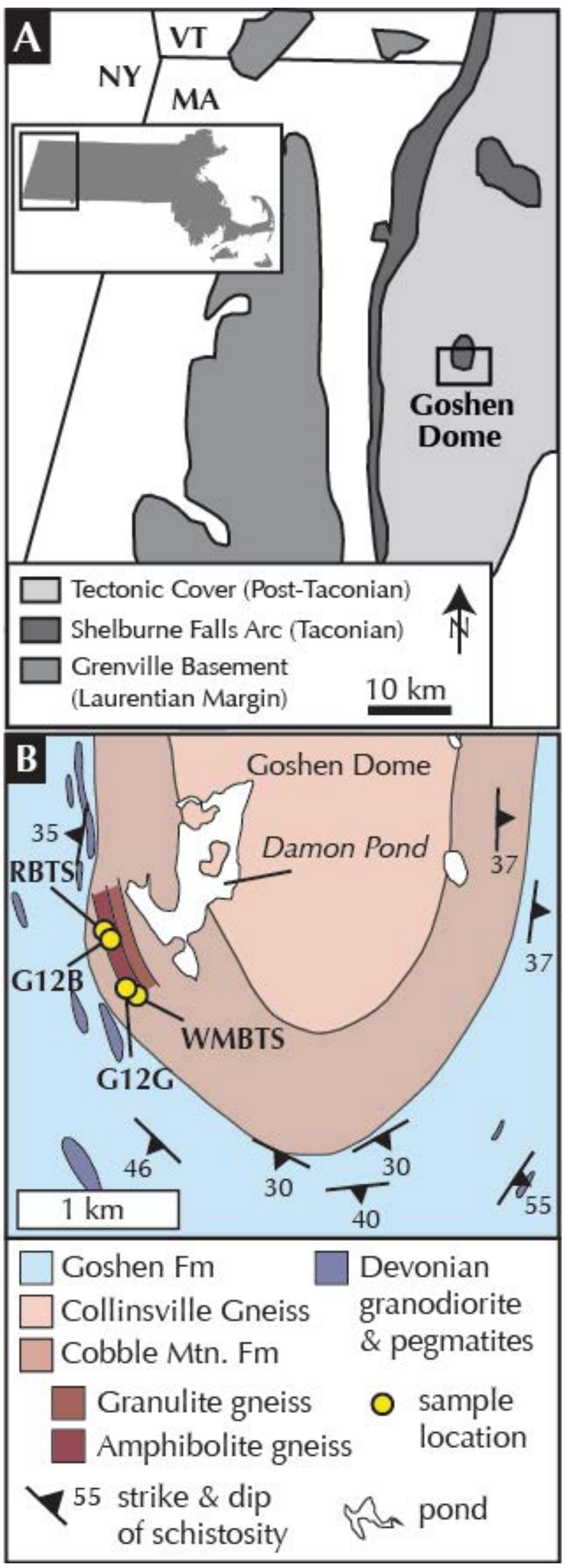
A
VT
NY
MA
Goshen Dome
Tectonic Cover (Post-Taconian)
Shelburne Falls Arc (Taconian)
Grenville Basement (Laurentian Margin)
N
10 km
B
Goshen Dome
Damon Pond
35
37
37
RBTS
G12B
WMBTS
G12G
46
30
30
40
55
1 km
Goshen Fm
Collinsville Gneiss
Cobble Mtn. Fm
Granulite gneiss
Amphibolite gneiss
Devonian granodiorite & pegmatites
sample location
55 strike & dip of schistosity
pond

Figure 1

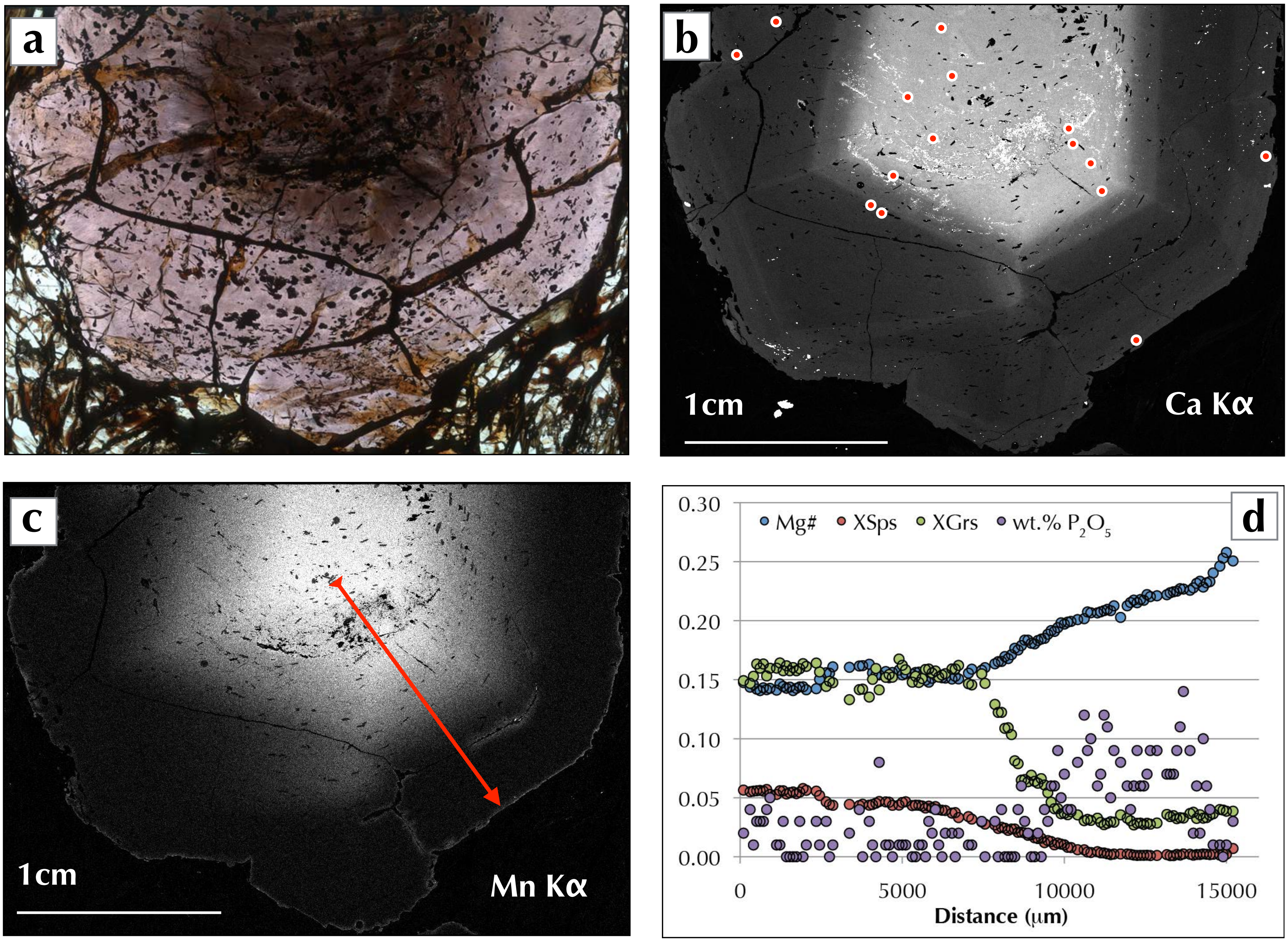
a
b
1cm
Ca Kα
c
1cm
Mn Kα
d
Mg#
XSps
XGrs
wt.% P_2O_5
0.30
0.25
0.20
0.15
0.10
0.05
0.00
0
5000
10000
15000
Distance (μm)

Figure 2

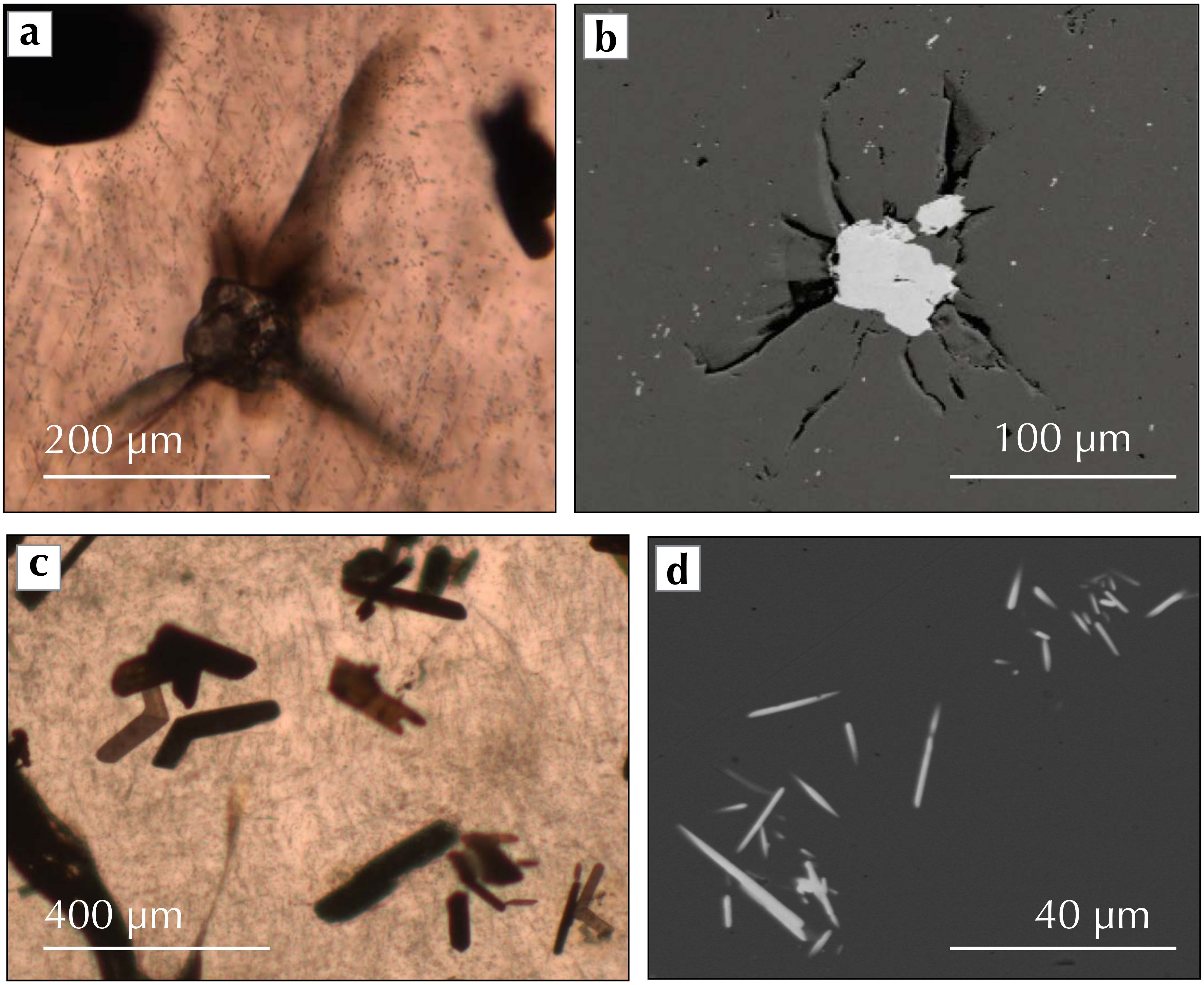

Figure 3

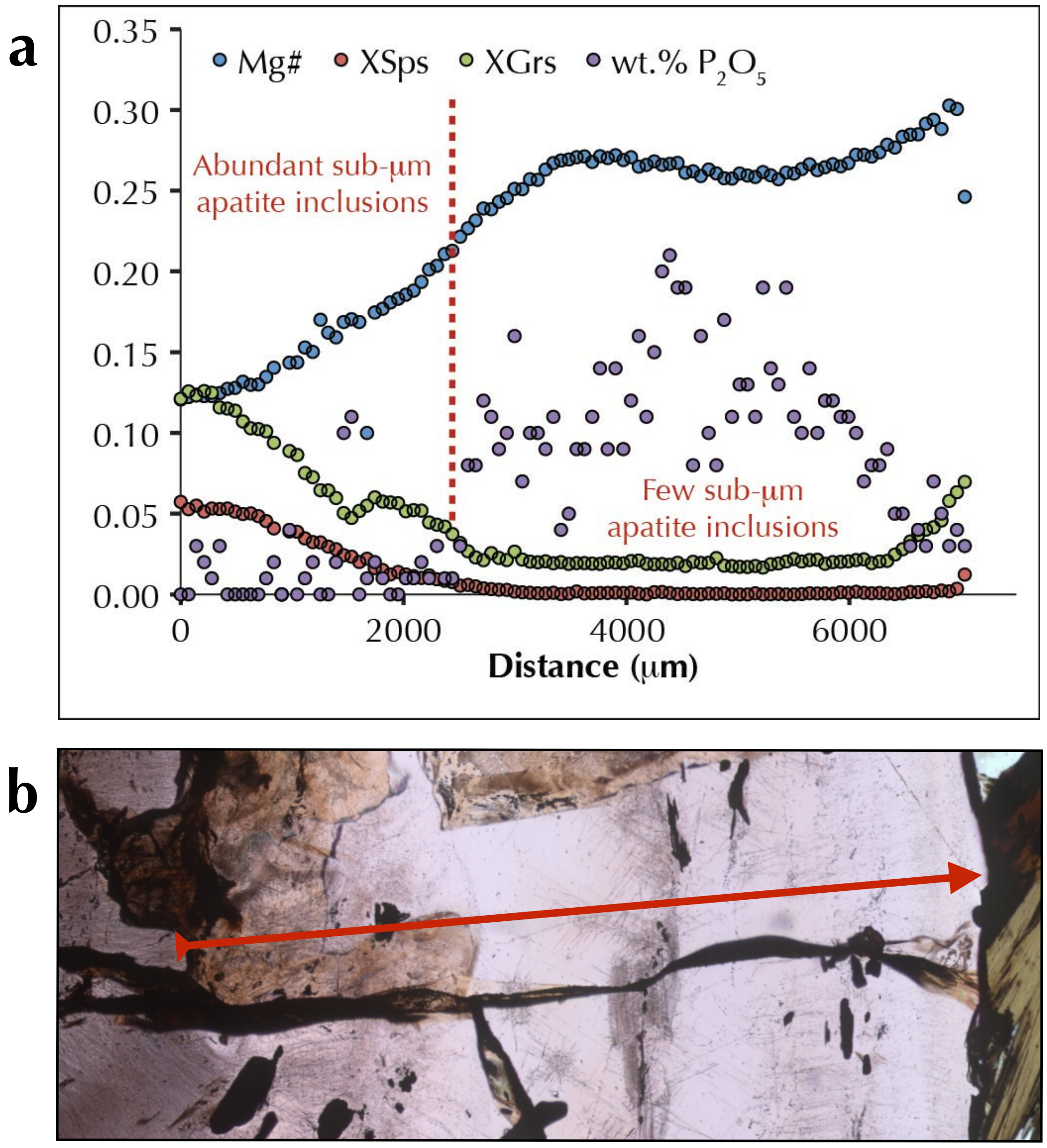
a
0.35
0.30
0.25
0.20
0.15
0.10
0.05
0.00
Mg#
XSps
XGrs
wt.% P2O5
Abundant sub-μm apatite inclusions
Few sub-μm apatite inclusions
0
2000
4000
6000
Distance (μm)
b

Figure 4

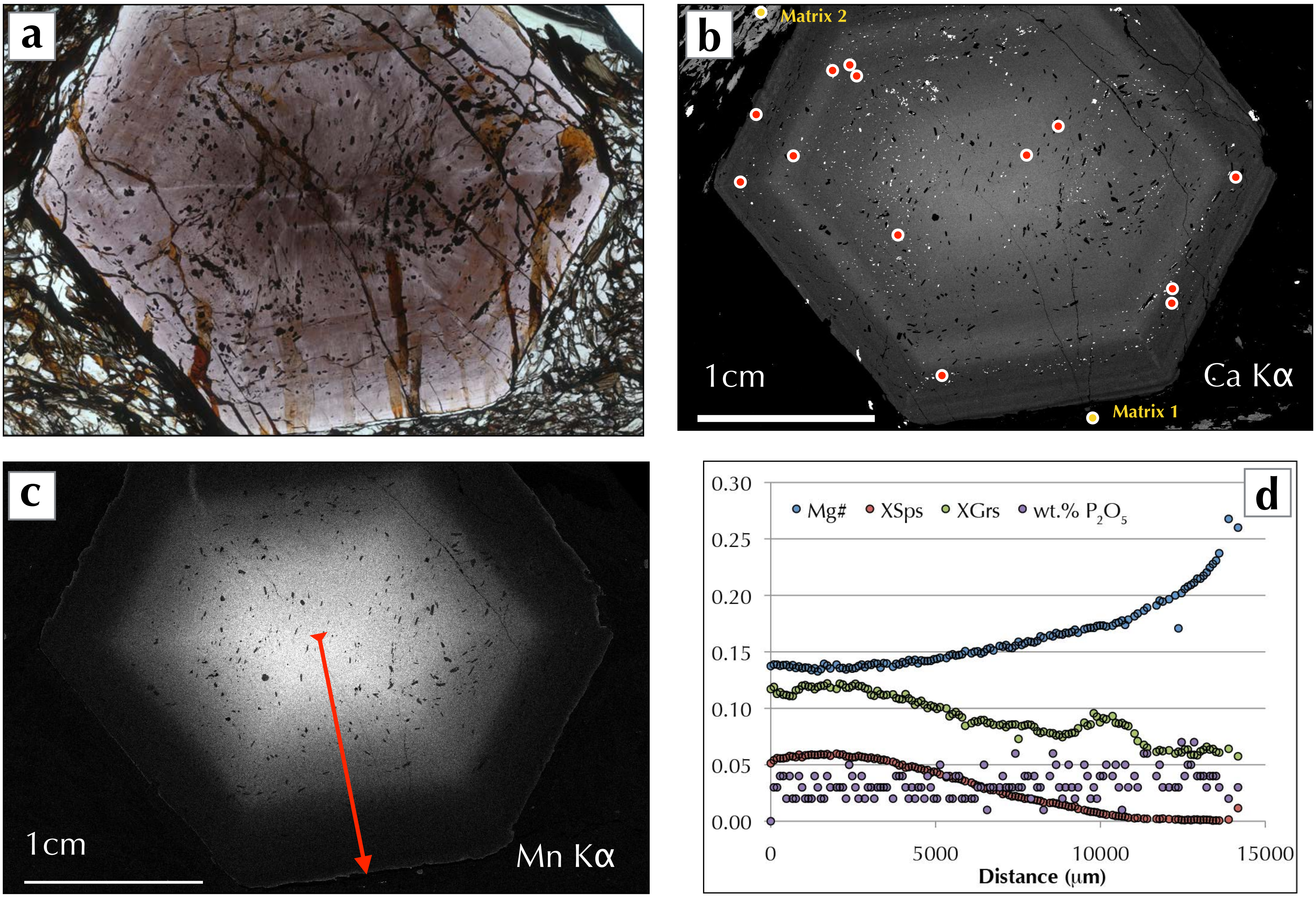
a
b
Matrix 2
Matrix 1
1cm
Ca Kα
c
1cm
Mn Kα
d
Mg#
XSps
XGrs
wt.% P2O5
0.30
0.25
0.20
0.15
0.10
0.05
0.00
0
5000
10000
15000
Distance (μm)

Figure 5

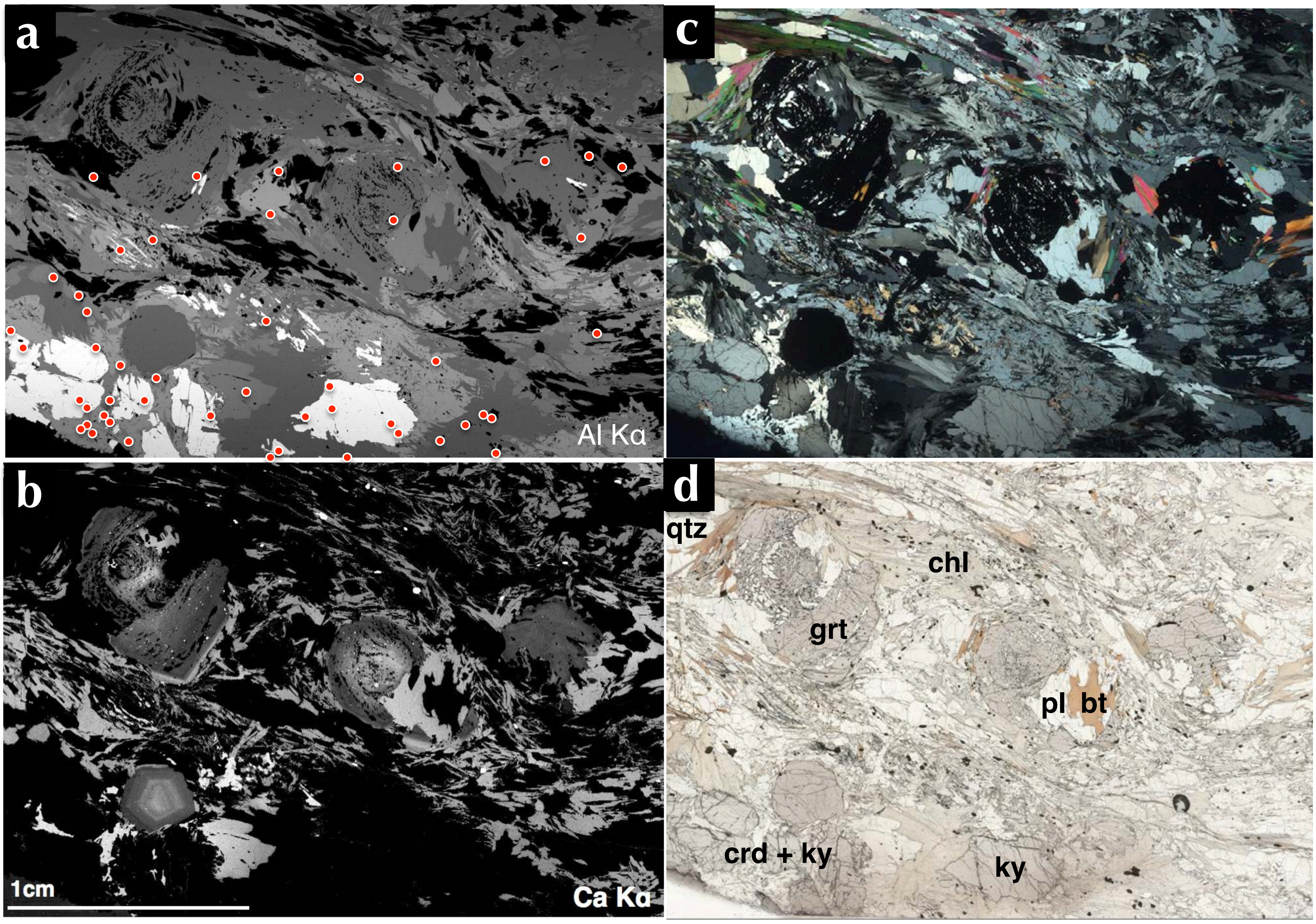

Figure 6

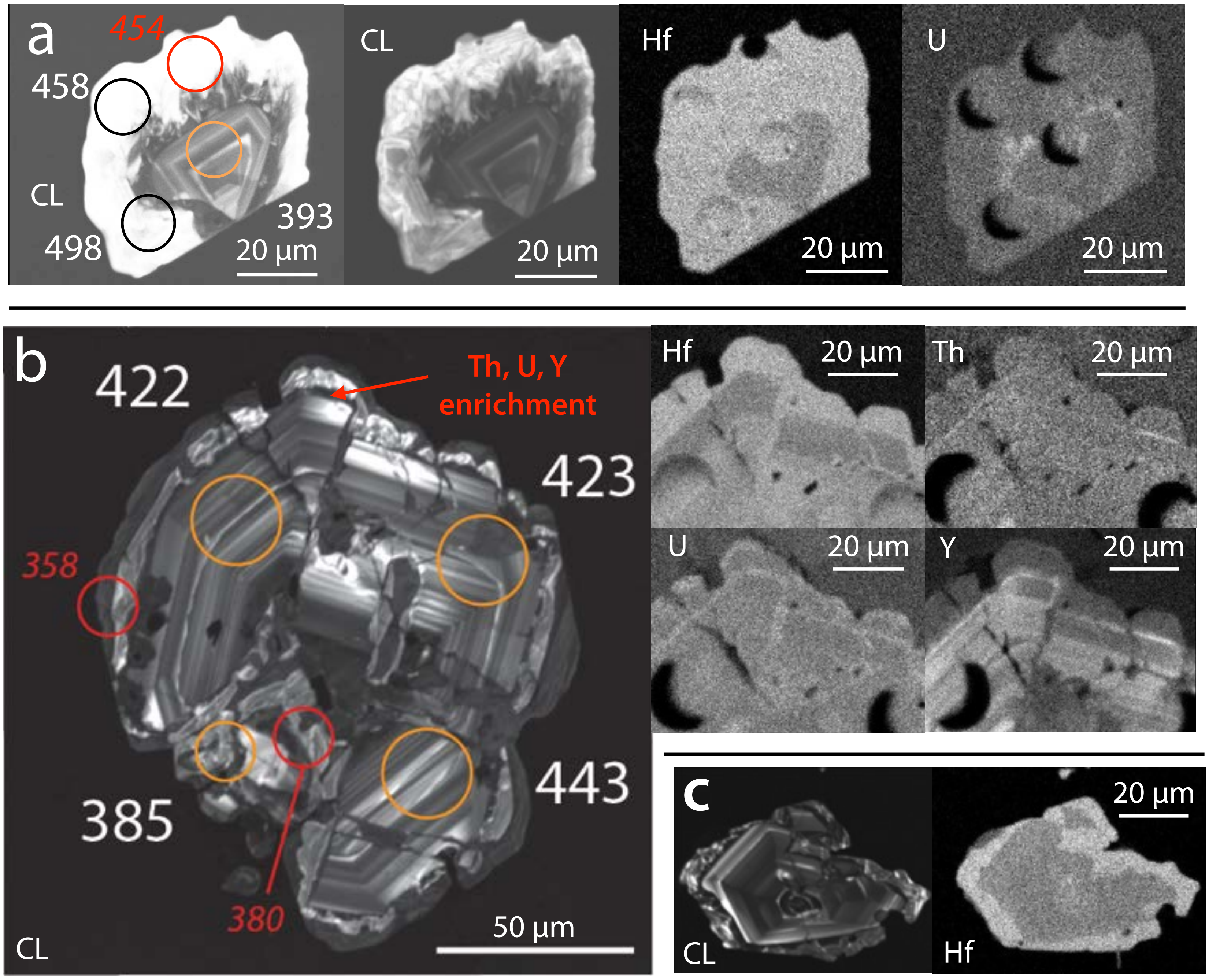

a
454
458
CL
498
393
20 µm
CL
20 µm
Hf
20 µm
U
20 µm
b
422
Th, U, Y
enrichment
423
358
385
443
380
CL
50 µm
Hf
20 µm
Th
20 µm
U
20 µm
Y
20 µm
c
CL
20 µm
Hf

Figure 7

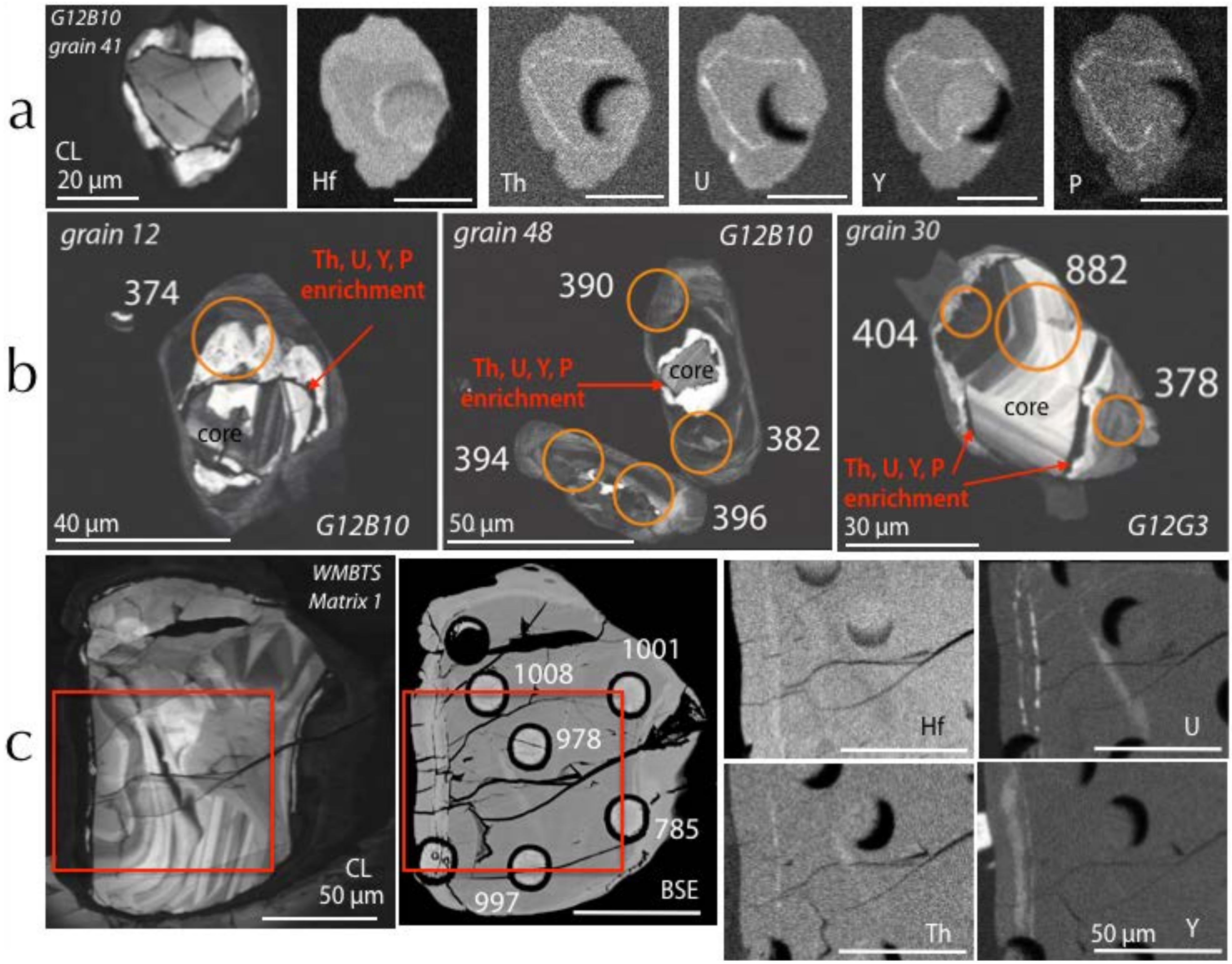

a
G12B10
grain 41
CL
20 µm
Hf
Th
U
Y
P
b
grain 12
374
Th, U, Y, P enrichment
core
40 µm
G12B10
grain 48
G12B10
390
Th, U, Y, P enrichment
core
382
394
396
50 µm
grain 30
882
404
378
core
Th, U, Y, P enrichment
30 µm
G12G3
c
WMBTS
Matrix 1
CL
50 µm
1001
1008
978
785
997
BSE
Hf
U
Th
50 µm
Y

Figure 8

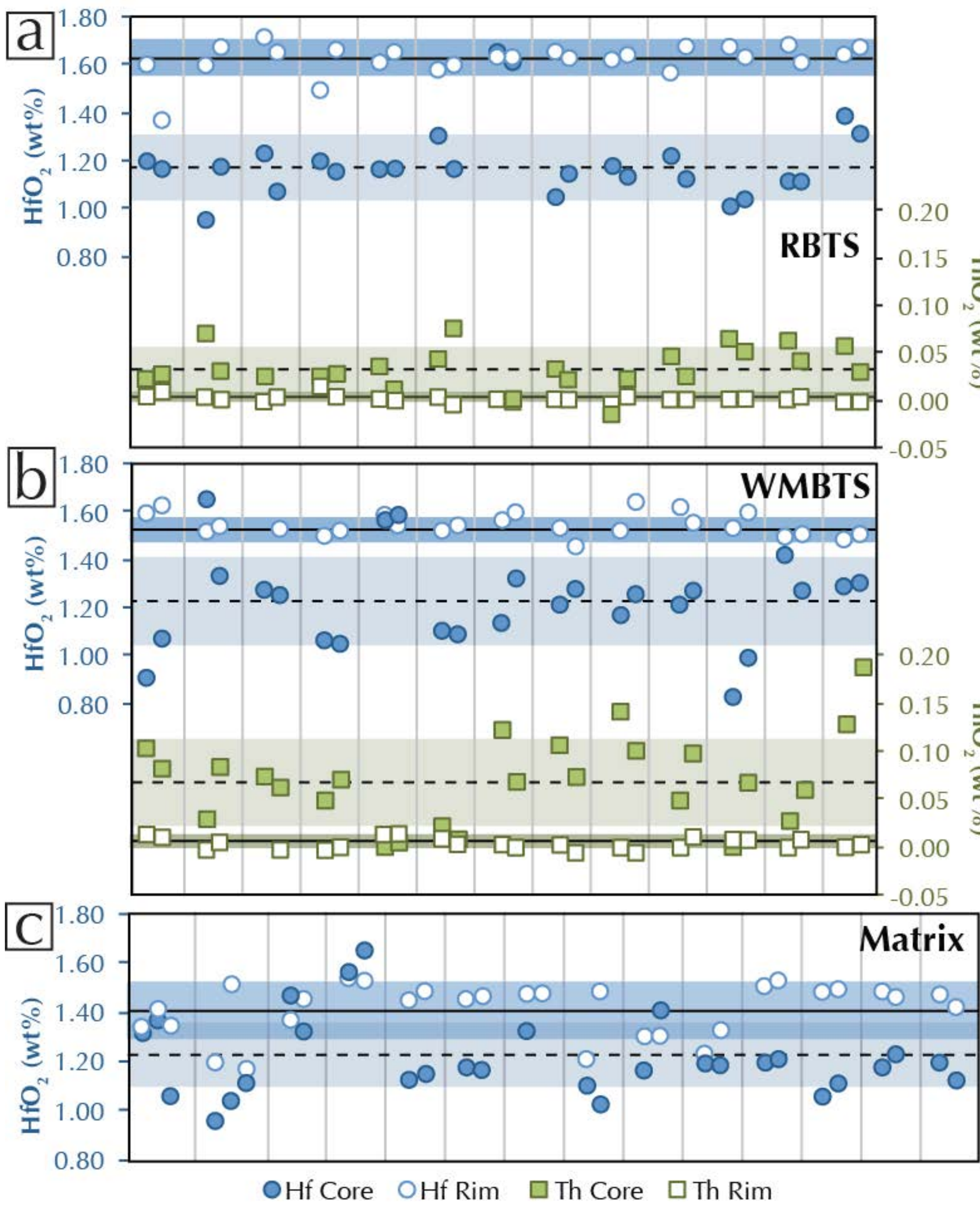
a
b
c
1.80
1.60
1.40
1.20
1.00
0.80
HfO2 (wt%)
0.20
0.15
0.10
0.05
0.00
-0.05
ThO2 (wt%)
RBTS
WMBTS
Matrix
Hf Core
Hf Rim
Th Core
Th Rim

Figure 9

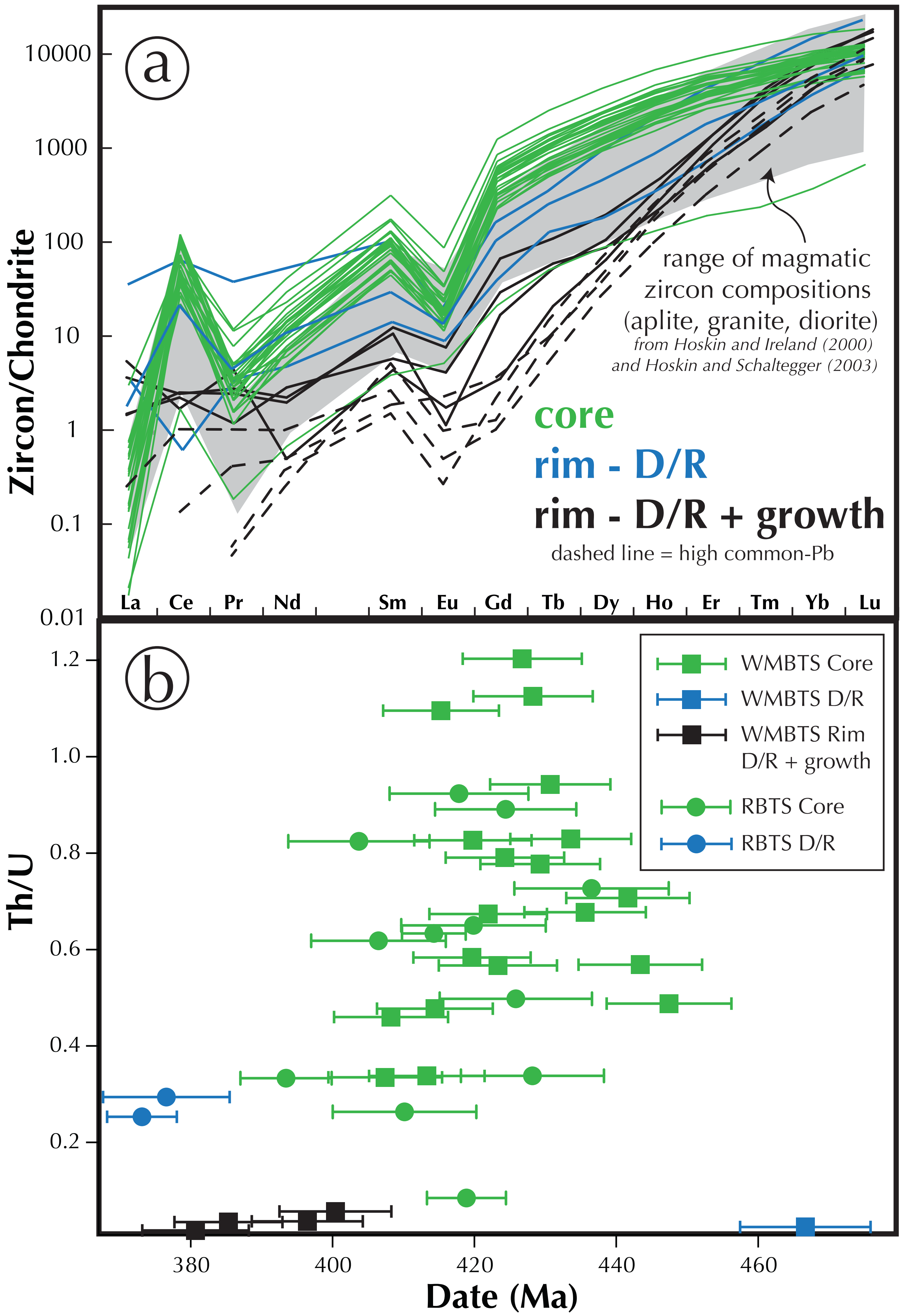

a
10000
1000
100
10
1
0.1
0.01
Zircon/Chondrite
range of magmatic
zircon compositions
(aplite, granite, diorite)
from Hoskin and Ireland (2000)
and Hoskin and Schaltegger (2003)
core
rim - D/R
rim - D/R + growth
dashed line = high common-Pb
La
Ce
Pr
Nd
Sm
Eu
Gd
Tb
Dy
Ho
Er
Tm
Yb
Lu
b
1.2
1.0
0.8
0.6
0.4
0.2
Th/U
WMBTS Core
WMBTS D/R
WMBTS Rim
D/R + growth
RBTS Core
RBTS D/R
380
400
420
440
460
Date (Ma)

Figure 10

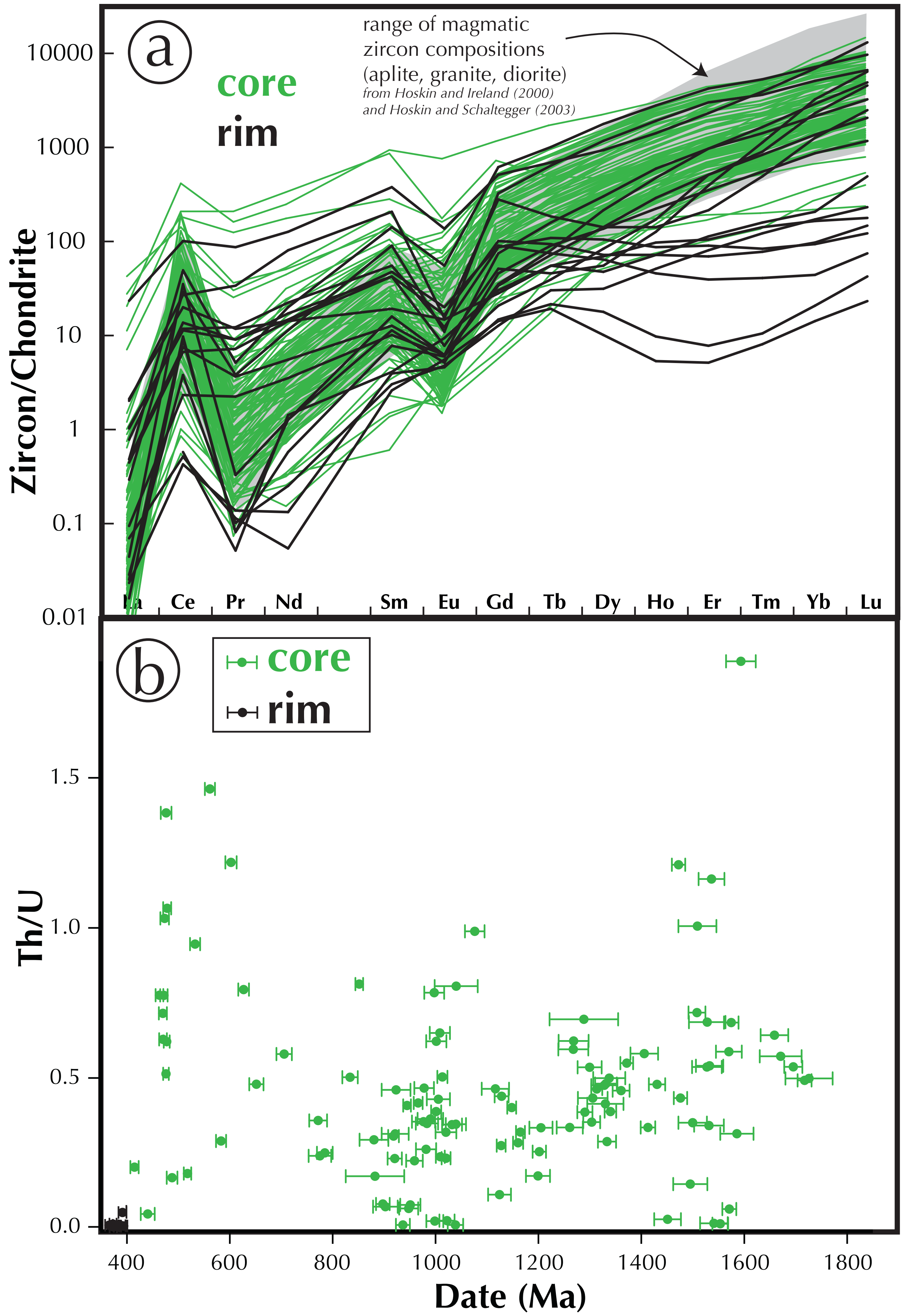

a
core
rim
range of magmatic
zircon compositions
(aplite, granite, diorite)
from Hoskin and Ireland (2000)
and Hoskin and Schaltegger (2003)
10000
1000
100
10
1
0.1
0.01
Zircon/Chondrite
Ce
Pr
Nd
Sm
Eu
Gd
Tb
Dy
Ho
Er
Tm
Yb
Lu
b
core
rim
1.5
1.0
0.5
0.0
Th/U
400
600
800
1000
1200
1400
1600
1800
Date (Ma)

Figure 11

										Preferred age (Ma)				
						238 /		207 /		207-corr Pb-			Pb-207/U-235	
		Source file			Err. Corr.	206	0.02	206	0.015	206/U-238	error 2s	disc.	Age	2 SE
Grt	Output_1_01	RoundBTS_zrn2	15um	C	0.886	14.57	0.35	0.055	0.001	428	10	1.01	424	5
Grt	Output_1_02	RoundBTS_zrn2	15um	C	0.929	14.93	0.36	0.056	0.001	418	10	0.99	421	5
Grt	Output_1_03	RoundBTS_zrn2	15um	C	0.912	15.36	0.37	0.055	0.001	406	9	0.99	410	4
Grt	Output_1_04	RoundBTS_zrn2	15um	C	0.930	15.46	0.39	0.055	0.001	404	10	0.99	408	5
Grt	Output_1_05	RoundBTS_zrn2	15um	C	0.909	14.27	0.36	0.056	0.001	437	11	1.00	437	6
Grt	Output_1_06	RoundBTS_zrn2	15um	MIX	0.944	16.16	0.42	0.056	0.001	387	10	0.98	395	6
Grt	Output_1_07	RoundBTS_zrn2	15um	MIX	0.924	16.14	0.37	0.056	0.001	387	9	0.98	396	4
Grt	Output_1_08	RoundBTS_zrn2	15um	D-R	0.934	16.61	0.40	0.055	0.001	377	9	0.99	381	5
Grt	Output_1_09	RoundBTS_zrn2	15um	C	0.887	14.84	0.37	0.056	0.001	420	10	0.99	425	6
Grt	Output_1_10	RoundBTS_zrn2	15um	C	0.892	14.64	0.38	0.055	0.001	426	11	0.99	428	7
Grt	Output_1_11	RoundBTS_zrn2	15um	C	0.777	15.22	0.38	0.055	0.001	410	10	1.00	412	6
Grt	Output_1_12	RoundBTS_zrn2	15um	C	0.881	14.67	0.35	0.057	0.001	424	10	0.98	434	5
Grt	Output_2_01	RoundBTS_zrn1	20um	MG	0.739	16.75	0.22	0.055	0.001	373	5	0.98	382	6
Grt	Output_2_03	RoundBTS_zrn1	20um	MG	0.759	11.19	0.75	0.059	0.003	552	36	1.00	553	38
Grt	Output_2_05	RoundBTS_zrn1	20um	C	0.790	15.06	0.17	0.055	0.001	414	4	1.00	413	5
Grt	Output_2_06	RoundBTS_zrn1	20um	C	0.550	14.90	0.20	0.055	0.001	419	6	1.00	417	6
Grt	Output_2_12	RoundBTS_zrn1	20um	MG	0.832	11.74	0.90	0.058	0.003	527	39	0.98	539	41
Grt	Output_2_13	RoundBTS_zrn1	20um	MIX	0.688	12.79	0.27	0.058	0.002	485	10	1.00	486	13
Grt	Output_2_14	RoundBTS_zrn1	20um	MIX	0.637	14.60	0.29	0.055	0.001	427	8	1.00	425	9
Grt	Output_2_16	RoundBTS_zrn1	20um	MG	0.722	12.42	0.47	0.060	0.002	498	18	0.99	506	22
Grt	Output_2_17	RoundBTS_zrn1	20um	MG	0.824	13.55	1.42	0.057	0.005	458	47	0.97	471	53
Grt	Output_2_19	RoundBTS_zrn1	20um	C	0.895	15.87	0.26	0.055	0.001	393	6	0.99	397	6
Grt	Output_1_01	WMBTS zir1		MG	0.861	15.60	0.43	0.055	0.001	400	8	1.00	399	9
Grt	Output_1_02	WMBTS zir1		C	0.814	15.06	0.39	0.055	0.001	414	8	1.00	415	6
Grt	Output_1_03	WMBTS zir1		C	0.845	15.30	0.36	0.055	0.001	408	8	1.00	407	5
Grt	Output_1_04	WMBTS zir1		MG	0.824	13.33	0.60	0.056	0.002	467	9	1.02	459	19
Grt	Output_1_05	WMBTS zir1		MG	0.629	15.75	0.39	0.056	0.001	396	8	0.98	407	7
Grt	Output_1_06	WMBTS z2		MG	0.614	16.42	0.39	0.055	0.001	381	8	0.98	387	7
Grt	Output_1_10	WMBTS z2		MIX	0.630	15.29	0.34	0.055	0.001	408	8	1.01	406	5
Grt	Output_1_11	WMBTS z3		C	0.791	14.85	0.33	0.056	0.001	420	8	1.00	421	4
Grt	Output_1_12	WMBTS z3		C	0.794	15.09	0.36	0.056	0.001	413	8	1.00	414	6
Grt	Output_1_13	WMBTS z3		MIX	0.719	15.76	0.37	0.056	0.001	396	8	0.99	399	5
Grt	Output_1_14	WMBTS z3		MIX	0.783	15.42	0.36	0.056	0.001	405	8	0.99	409	5

Grt	Output_1_16	WMBTS z4	MIX	0.913	16.00	0.44	0.057	0.001	**390**	**8**	0.98	399	6
Grt	Output_1_17	WMBTS z4	MIX	0.731	15.55	0.36	0.056	0.001	**401**	**8**	0.99	404	5
Grt	Output_1_18	WMBTS z4	C	0.769	14.11	0.31	0.055	0.001	**442**	**9**	1.01	436	4
Grt	Output_1_19	WMBTS z4	C	0.369	14.37	0.29	0.056	0.001	**434**	**9**	1.01	429	2
Grt	Output_1_20	WMBTS z4	C	0.774	14.47	0.32	0.056	0.001	**431**	**8**	1.01	427	4
Grt	Output_1_21	WMBTS z5	MIX	0.539	15.89	0.34	0.056	0.001	**393**	**8**	0.99	397	4
Grt	Output_1_22	WMBTS z5	C	0.795	14.29	0.32	0.056	0.001	**436**	**9**	1.00	437	5
Grt	Output_1_24	WMBTS z6	C	0.591	14.86	0.31	0.055	0.001	**420**	**8**	1.01	417	4
Grt	Output_1_25	WMBTS z6	MIX	0.451	12.80	0.32	0.057	0.001	**485**	**10**	1.01	482	9
Grt	Output_1_28	WMBTS z8	MIX	0.880	15.49	0.35	0.055	0.001	**403**	**8**	1.01	399	5
Grt	Output_1_29	WMBTS z9	C	0.557	14.56	0.30	0.055	0.001	**428**	**8**	1.01	425	3
Grt	Output_1_31	WMBTS z10	MG	0.290	16.19	0.38	0.056	0.001	**385**	**8**	0.98	395	5
Grt	Output_2_01	WMBTS Spot 15	C	0.856	14.52	0.34	0.055	0.001	**429**	**8**	1.00	429	4
Grt	Output_2_03	WMBTS Spot 17	C	0.796	14.06	0.31	0.055	0.001	**443**	**9**	1.02	435	4
Grt	Output_2_04	WMBTS Spot 18	C	0.812	14.78	0.33	0.055	0.001	**422**	**8**	1.00	421	4
Grt	Output_2_05	WMBTS Spot 19	C	0.882	14.73	0.34	0.055	0.001	**423**	**8**	1.00	424	4
Grt	Output_2_07	WMBTS Spot 21	C	0.882	14.62	0.32	0.055	0.001	**427**	**8**	1.01	423	3
Ma	Output_2_09	WMBTS Spot 23	C	0.510	5.98	0.13	0.072	0.002	**997**	**19**	1.00	993	8
Ma	Output_2_10	WMBTS Spot 24	C	0.994	7.70	0.43	0.068	0.002	**785**	**15**	0.99	794	32
Ma	Output_2_11	WMBTS Spot 25	C	0.846	5.95	0.14	0.072	0.001	**1001**	**19**	1.01	994	7
Ma	Output_2_12	WMBTS Spot 26	C	0.824	6.10	0.14	0.072	0.002	**978**	**19**	1.00	982	7
Ma	Output_2_13	WMBTS Spot 27	C	0.778	5.91	0.14	0.073	0.002	**1008**	**20**	1.00	1006	9
Grt	Output_2_15	WMBTS Spot 29	C	0.826	15.02	0.33	0.055	0.001	**415**	**8**	0.99	419	4
Grt	Output_2_16	WMBTS Spot 30	C	0.859	15.31	0.35	0.056	0.001	**407**	**8**	0.99	410	4
Grt	Output_2_17	WMBTS Spot 31	C	0.867	13.93	0.34	0.055	0.001	**447**	**9**	1.01	441	5
Grt	Output_2_18	WMBTS Spot 32	C	0.804	14.70	0.33	0.055	0.001	**424**	**8**	1.00	422	4
Ma	Output_1_01	G12G3_zrn 20um	C	0.892	6.32	0.05	0.072	0.001	**945**	**8**	0.98	962	5
Ma	Output_1_03	G12G3_zrn 20um	C	0.962	4.46	0.06	0.085	0.001	**1304**	**16**	1.00	1306	7
Ma	Output_1_04	G12G3_zrn 20um	C	0.995	4.63	0.10	0.083	0.001	**1261**	**25**	1.00	1263	15
Ma	Output_1_07	G12G3_zrn 20um	C	0.746	5.13	0.04	0.079	0.001	**1148**	**9**	1.00	1154	6
Ma	Output_1_08	G12G3_zrn 20um	C	0.813	3.89	0.03	0.094	0.001	**1472**	**13**	0.99	1488	7
Ma	Output_1_09	G12G3_zrn 20um	C	0.981	12.69	0.27	0.059	0.001	**488**	**10**	0.97	502	9
Ma	Output_1_11	G12G3_zrn 20um	C	0.865	4.23	0.04	0.085	0.001	**1372**	**13**	1.01	1351	7
Ma	Output_1_12	G12G3_zrn 20um	C	0.845	5.22	0.04	0.078	0.001	**1128**	**9**	0.99	1140	5
Ma	Output_1_13	G12G3_zrn 20um	C	0.753	5.05	0.04	0.078	0.001	**1165**	**9**	1.00	1168	7
Ma	Output_1_14	G12G3_zrn 20um	C	0.867	5.07	0.04	0.079	0.001	**1160**	**10**	0.99	1171	8

Ma	Output_1_15	G12G3_zrn	20um	C	0.828	3.29	0.03	0.103	0.001	**1717**	**14**	1.01	1699	8
Ma	Output_1_16	G12G3_zrn	20um	C	0.833	3.59	0.03	0.103	0.001	**1575**	**14**	0.97	1625	8
Ma	Output_1_17	G12G3_zrn	20um	C	0.894	3.33	0.03	0.104	0.001	**1695**	**17**	1.00	1702	10
Ma	Output_1_18	G12G3_zrn	20um	C	0.838	6.17	0.06	0.073	0.001	**966**	**9**	0.99	982	7
Ma	Output_1_19	G12G3_zrn	20um	C	0.790	5.95	0.06	0.072	0.001	**1001**	**10**	0.99	1007	8
Ma	Output_1_20	G12G3_zrn	20um	C	0.843	3.88	0.03	0.094	0.001	**1476**	**13**	0.99	1491	8
Ma	Output_1_21	G12G3_zrn	20um	C	0.910	4.08	0.04	0.090	0.001	**1413**	**14**	0.99	1424	9
Ma	Output_1_22	G12G3_zrn	20um	C	0.876	3.60	0.03	0.102	0.001	**1571**	**13**	0.98	1618	6
Ma	Output_1_23	G12G3_zrn	20um	C	0.598	13.02	0.16	0.056	0.001	**478**	**6**	1.01	474	6
Ma	Output_1_24	G12G3_zrn	20um	C	0.892	4.43	0.04	0.084	0.001	**1313**	**11**	1.00	1310	7
Ma	Output_1_25	G12G3_zrn	20um	C	0.937	4.51	0.05	0.084	0.001	**1290**	**15**	1.00	1286	8
Ma	Output_1_26	G12G3_zrn	20um	C	0.892	4.34	0.04	0.084	0.001	**1340**	**11**	1.01	1323	8
Ma	Output_1_27	G12G3_zrn	20um	C	0.931	5.20	0.06	0.082	0.001	**1128**	**14**	0.97	1172	9
Ma	Output_1_28	G12G3_zrn	20um	C	0.997	6.78	0.45	0.072	0.001	**882**	**57**	0.97	909	51
Ma	Output_1_30	G12G3_zrn	20um	C	0.882	7.06	0.06	0.070	0.001	**852**	**8**	0.98	875	8
Ma	Output_1_31	G12G3_zrn	20um	C	0.887	4.24	0.05	0.091	0.001	**1361**	**16**	0.98	1394	13
Ma	Output_1_32	G12G3_zrn	20um	C	0.811	3.67	0.04	0.096	0.001	**1553**	**15**	1.00	1551	8
Ma	Output_1_33	G12G3_zrn	20um	C	0.913	5.89	0.06	0.071	0.001	**1013**	**10**	1.02	990	6
Ma	Output_1_34	G12G3_zrn	20um	C	0.867	11.96	0.17	0.057	0.001	**518**	**7**	1.01	515	7
Ma	Output_1_35	G12G3_zrn	20um	C	0.675	13.05	0.16	0.056	0.001	**476**	**6**	1.00	476	6
Ma	Output_1_38	G12G3_zrn	20um	C	0.784	4.85	0.05	0.084	0.001	**1202**	**13**	0.97	1240	10
Ma	Output_1_39	G12G3_zrn	20um	C	0.839	4.36	0.06	0.085	0.001	**1333**	**18**	1.00	1328	12
Ma	Output_1_40	G12G3_zrn	20um	C	0.880	3.80	0.04	0.094	0.001	**1508**	**16**	1.00	1508	9
Ma	Output_1_41	G12G3_zrn	20um	C	0.835	5.83	0.05	0.073	0.001	**1021**	**9**	1.00	1018	8
Ma	Output_1_42	G12G3_zrn	20um	C	0.615	5.90	0.05	0.073	0.001	**1009**	**9**	1.00	1010	7
Ma	Output_1_43	G12G3_zrn	20um	C	0.794	6.53	0.08	0.070	0.001	**918**	**10**	0.99	924	8
Ma	Output_1_44	G12G3_zrn	20um	C	0.851	4.03	0.05	0.090	0.001	**1430**	**16**	1.00	1430	9
Ma	Output_1_05	G12G3_zrn3	15um	C	0.923	3.38	0.08	0.103	0.002	**1671**	**41**	1.00	1673	11
Ma	Output_1_06	G12G3_zrn3	15um	C	0.896	3.27	0.09	0.103	0.002	**1726**	**46**	1.01	1703	16
Ma	Output_1_07	G12G3_zrn3	15um	C	0.890	3.85	0.09	0.090	0.002	**1495**	**33**	1.01	1470	9
Ma	Output_1_08	G12G3_zrn3	15um	C	0.951	6.51	0.19	0.070	0.001	**921**	**26**	0.99	928	14
Ma	Output_1_09	G12G3_zrn3	15um	C	0.915	6.02	0.16	0.073	0.002	**990**	**25**	0.99	996	11
Ma	Output_1_10	G12G3_zrn3	15um	C	0.918	6.11	0.15	0.072	0.001	**976**	**23**	0.99	986	8
Ma	Output_1_11	G12G3_zrn3	15um	C	0.950	6.06	0.14	0.073	0.001	**983**	**22**	0.99	994	8
Ma	Output_1_12	G12G3_zrn3	15um	C	0.962	6.49	0.20	0.071	0.002	**923**	**28**	0.99	937	17
Ma	Output_1_15	G12G3_zrn3	15um	C	0.979	4.59	0.11	0.085	0.002	**1268**	**29**	0.99	1284	9

Ma	Output_1_16	G12G3_zrn3	15um	C	0.966	4.46	0.10	0.084	0.002	**1306**	**29**	1.01	1296	9
Ma	Output_1_17	G12G3_zrn3	15um	C	0.980	5.68	0.24	0.078	0.002	**1040**	**42**	0.97	1074	28
Ma	Output_1_18	G12G3_zrn3	15um	C	0.976	4.35	0.10	0.084	0.002	**1338**	**31**	1.02	1312	10
Ma	Output_1_19	G12G3_zrn3	15um	C	0.972	5.26	0.13	0.081	0.002	**1116**	**27**	0.98	1149	11
Ma	Output_1_20	G12G3_zrn3	15um	D-R	0.879	16.58	0.49	0.053	0.001	**378**	**11**	1.02	370	8
Ma	Output_1_21	G12G3_zrn3	15um	MIX	0.934	15.46	0.39	0.055	0.001	**404**	**10**	1.01	402	5
Ma	Output_1_23	G12G3_zrn3	15um	C	0.898	3.80	0.09	0.093	0.002	**1509**	**37**	1.01	1496	11
Ma	Output_1_24	G12G3_zrn3	15um	C	0.993	4.48	0.24	0.090	0.002	**1288**	**67**	0.97	1337	43
Ma	Output_1_25	G12G3_zrn3	15um	C	0.896	3.75	0.09	0.092	0.002	**1528**	**35**	1.02	1497	10
Ma	Output_1_26	G12G3_zrn3	15um	C	0.956	6.63	0.18	0.072	0.002	**903**	**24**	0.97	932	14
Ma	Output_1_27	G12G3_zrn3	15um	C	0.865	7.81	0.23	0.067	0.002	**775**	**22**	0.99	788	15
Ma	Output_1_28	G12G3_zrn3	15um	C	0.907	6.84	0.22	0.068	0.002	**880**	**28**	1.01	874	18
Ma	Output_1_29	G12G3_zrn3	15um	C	0.954	4.35	0.12	0.088	0.002	**1330**	**35**	0.99	1348	13
Ma	Output_1_01	G12B10_z	15um	MIX	0.903	16.34	0.35	0.056	0.001	**382**	**8**	0.97	395	5
Ma	Output_1_07	G12B10_z	15um	C	0.923	4.85	0.09	0.083	0.002	**1205**	**23**	0.98	1235	8
Ma	Output_1_08	G12B10_z	15um	C	0.966	4.88	0.10	0.082	0.002	**1199**	**23**	0.98	1221	9
Ma	Output_1_09	G12B10_z	15um	C	0.970	6.28	0.13	0.073	0.001	**951**	**20**	0.98	976	9
Ma	Output_1_10	G12B10_z	15um	D-R	0.900	16.71	0.33	0.056	0.001	**374**	**7**	0.97	388	4
Ma	Output_1_12	G12B10_z	15um	C	0.962	3.74	0.07	0.096	0.002	**1527**	**29**	0.99	1543	9
Ma	Output_1_14	G12B10_z	15um	D-R	0.888	16.78	0.32	0.054	0.001	**373**	**7**	0.99	377	4
Ma	Output_1_16	G12B10_z	15um	MIX	0.886	15.60	0.31	0.054	0.001	**401**	**8**	1.00	399	4
Ma	Output_1_21	G12B10_z	15um	D-R	0.876	15.97	0.33	0.055	0.001	**391**	**8**	0.98	398	5
Ma	Output_1_26	G12B10_z	15um	Patch	0.740	15.48	0.30	0.055	0.001	**403**	**8**	1.00	402	5
Ma	Output_1_27	G12B10_z	15um	Patch	0.731	15.71	0.30	0.055	0.001	**398**	**7**	1.00	398	4
Ma	Output_1_28	G12B10_z	15um	Patch	0.937	16.30	0.32	0.054	0.001	**384**	**7**	1.00	382	4
Ma	Output_1_29	G12B10_z	15um	C	0.932	7.85	0.18	0.066	0.001	**772**	**17**	0.99	781	10
Ma	Output_1_32	G12B10_z	15um	C	0.870	4.08	0.08	0.093	0.002	**1406**	**27**	0.99	1433	9
Ma	Output_1_33	G12B10_z	15um	C	0.972	3.75	0.07	0.092	0.002	**1532**	**29**	1.02	1494	8
Ma	Output_1_35	G12B10_z	15um	D-R	0.895	15.91	0.29	0.054	0.001	**393**	**7**	1.01	390	4
Ma	Output_1_36	G12B10_z	15um	C	0.914	7.21	0.13	0.070	0.001	**834**	**15**	0.97	860	6
Ma	Output_1_44	G12B10_z	15um	C	0.860	13.05	0.29	0.056	0.001	**476**	**10**	1.01	474	7
Ma	Output_1_46	G12B10_z	15um	C	0.965	9.42	0.21	0.060	0.001	**652**	**14**	1.01	643	7
Ma	Output_1_47	G12B10_z	15um	D-R	0.796	16.76	0.32	0.055	0.001	**373**	**7**	0.98	382	4
Ma	Output_1_49	G12B10_z	15um	C	0.941	4.59	0.11	0.084	0.002	**1268**	**29**	0.99	1280	14
Ma	Output_1_51	G12B10_z	15um	MIX	0.845	16.61	0.35	0.055	0.001	**377**	**8**	0.99	382	5
Ma	Output_1_57	G12B10_z	15um	C	0.928	3.81	0.07	0.096	0.002	**1500**	**28**	0.99	1514	9

Ma	Output_1_59	G12B10_z 15um	C	0.995	14.12	0.44	0.056	0.001	**441**	**13**	1.00	442	9
Ma	Output_1_65	G12B10_z 15um	C	0.871	11.60	0.22	0.059	0.001	**533**	**10**	0.99	537	4
Ma	Output_1_67	G12B10_z 15um	C	0.969	5.21	0.11	0.083	0.002	**1124**	**22**	0.97	1171	10
Ma	Output_1_70	G12B10_z 15um	C	0.924	4.48	0.08	0.085	0.002	**1299**	**23**	1.00	1298	7
Ma	Output_1_72	G12B10_z 15um	D-R	0.812	15.98	0.29	0.056	0.001	**390**	**7**	0.98	400	4
Ma	Output_1_74	G12B10_z 15um	D-R	0.868	16.37	0.30	0.056	0.001	**382**	**7**	0.98	391	3
Ma	Output_1_75	G12B10_z 15um	MIX	0.898	15.75	0.29	0.056	0.001	**396**	**7**	0.98	404	4
Ma	Output_1_76	G12B10_z 15um	D-R	0.883	15.87	0.30	0.055	0.001	**394**	**7**	1.00	393	3
Ma	Output_1_77	G12B10_z 15um	Patch	0.819	17.15	0.32	0.055	0.001	**365**	**7**	0.99	371	4
Ma	Output_1_79	G12B10_z 15um	C	0.919	8.62	0.19	0.065	0.001	**706**	**15**	0.98	724	8
Ma	Output_1_81	G12B10_z 15um	C	0.877	4.37	0.09	0.085	0.002	**1328**	**25**	1.00	1322	9
Ma	Output_1_86	G12B10_z 15um	C	0.877	10.22	0.19	0.059	0.001	**602**	**11**	1.01	597	5
Ma	Output_1_87	G12B10_z 15um	C	0.864	10.99	0.20	0.058	0.001	**562**	**10**	1.00	561	4
Ma	Output_1_88	G12B10_z 15um	D-R	0.812	17.15	0.36	0.054	0.001	**365**	**7**	0.99	370	4
Ma	Output_1_89	G12B10_z 15um	C	0.946	15.06	0.29	0.055	0.001	**415**	**8**	1.01	412	4
Ma	Output_1_90	G12B10_z 15um	D-R	0.875	15.90	0.31	0.055	0.001	**393**	**8**	0.99	396	4
Ma	Output_1_91	G12B10_z 15um	C	0.975	6.30	0.13	0.072	0.001	**948**	**18**	0.99	963	7
Ma	Output_1_93	G12B10_z 15um	C	0.860	6.08	0.12	0.072	0.001	**981**	**20**	1.00	984	8
Ma	Output_1_96	G12B10_z 15um	C	0.733	5.92	0.14	0.074	0.002	**1005**	**22**	0.99	1013	14
Ma	Output_1_101	G12B10_z 15um	C	0.921	5.83	0.12	0.073	0.001	**1020**	**20**	1.01	1012	10
Ma	Output_1_102	G12B10_z 15um	D-R	0.815	14.33	0.26	0.057	0.001	**434**	**8**	0.97	448	4
Ma	Output_1_103	G12B10_z 15um	C	0.900	5.72	0.11	0.073	0.001	**1040**	**20**	1.01	1033	7
Ma	Output_1_104	G12B10_z 15um	C	0.916	5.76	0.11	0.073	0.001	**1032**	**19**	1.01	1025	8
Ma	Output_1_01	G12B8_z 15um	C	0.895	3.40	0.06	0.103	0.001	**1659**	**27**	1.00	1668	10
Ma	Output_1_03	G12B8_z 15um	C	0.906	5.82	0.09	0.073	0.001	**1022**	**15**	1.01	1016	6
Ma	Output_1_04	G12B8_z 15um	C	0.964	5.97	0.10	0.072	0.001	**999**	**16**	1.00	995	8
Ma	Output_1_07	G12B8_z 15um	C	0.951	5.72	0.08	0.074	0.001	**1039**	**15**	1.00	1041	6
Ma	Output_1_08	G12B8_z 15um	C	0.930	6.40	0.10	0.070	0.001	**936**	**14**	1.01	929	6
Ma	Output_1_11	G12B8_z 15um	C	0.973	3.72	0.07	0.093	0.001	**1541**	**27**	1.02	1513	11
Ma	Output_1_12	G12B8_z 15um	C	0.972	3.60	0.07	0.095	0.001	**1586**	**32**	1.01	1560	13
Ma	Output_1_13	G12B8_z 15um	C	0.967	3.57	0.07	0.098	0.001	**1594**	**29**	1.00	1593	14
Ma	Output_1_14	G12B8_z 15um	C	0.967	3.95	0.07	0.093	0.001	**1451**	**26**	0.99	1468	12
Ma	Output_1_17	G12B8_z 15um	C	0.841	6.51	0.10	0.071	0.001	**921**	**14**	0.99	929	6
Ma	Output_1_19	G12B8_z 15um	C	0.824	10.57	0.18	0.059	0.001	**583**	**10**	1.01	577	6
Ma	Output_1_20	G12B8_z 15um	D-R	0.876	15.43	0.23	0.055	0.001	**405**	**6**	1.00	406	3
Ma	Output_1_21	G12B8_z 15um	C	0.943	5.48	0.10	0.079	0.001	**1076**	**19**	0.97	1116	10

Ma	Output_1_22	G12B8_z	15um	C	0.965	6.68	0.10	0.070	0.001	**897**	**13**	0.99	909	6
Ma	Output_1_23	G12B8_z	15um	Patch	0.982	14.97	0.50	0.056	0.001	**416**	**14**	0.97	428	16
Ma	Output_1_24	G12B8_z	15um	C	0.912	9.78	0.16	0.062	0.001	**627**	**10**	0.98	639	6
Ma	Output_1_26	G12B8_z	15um	MIX	0.860	15.83	0.26	0.057	0.001	**394**	**6**	0.97	407	4
Ma	Output_1_27	G12B8_z	15um	C	0.884	6.24	0.11	0.071	0.001	**959**	**16**	1.01	955	11
Ma	Output_1_28	G12B8_z	15um	C	0.916	3.72	0.07	0.096	0.001	**1533**	**27**	0.99	1542	11
Ma	Output_1_29	G12B8_z	15um	C	0.951	3.64	0.06	0.095	0.001	**1570**	**25**	1.01	1551	10
Ma	Output_1_30	G12B8_z	15um	C	0.948	3.71	0.06	0.096	0.001	**1536**	**25**	1.00	1541	10
Ma	Output_1_31	G12B8_z	15um	C	0.776	13.23	0.22	0.056	0.001	**470**	**8**	1.02	462	5
Ma	Output_1_32	G12B8_z	15um	C	0.776	13.16	0.21	0.057	0.001	**472**	**7**	0.99	475	5
Ma	Output_1_33	G12B8_z	15um	C	0.866	13.42	0.22	0.056	0.001	**463**	**7**	1.01	461	5
Ma	Output_1_34	G12B8_z	15um	C	0.867	13.12	0.23	0.056	0.001	**474**	**8**	1.01	471	6
Ma	Output_1_35	G12B8_z	15um	C	0.720	13.23	0.22	0.056	0.001	**470**	**8**	1.01	464	5
Ma	Output_1_36	G12B8_z	15um	C	0.858	13.00	0.22	0.056	0.001	**478**	**8**	1.02	470	6
Ma	Output_1_37	G12B8_z	15um	C	0.910	4.37	0.07	0.083	0.001	**1331**	**21**	1.02	1308	9
Ma	Output_1_40	G12B8_z	15um	Patch	0.875	15.71	0.27	0.057	0.001	**397**	**7**	0.97	411	5
Ma	Output_1_41	G12B8_z	15um	MIX	0.959	13.76	0.27	0.056	0.001	**452**	**9**	1.00	453	6

Flagged for Pb-common
C = core
D-R = dissolution-reprecipitation
MG = metamorphic growth of new material
MIX = mixing 2+ domains
Patchy = textural pattern
Grt = within garnet megacryst
Ma = within matrix

Pb-206/U-238 Age	2 SE	Pb-207/Pb-206 Age	2 SE	Approx U (ppm)	Approx Th (ppm)	Approx Pb (ppm)	Pb-206/Pb-204	Ti (ppm)	Y (ppm)	La (ppm)	Ce (ppm)	Pr (ppm)	Nd (ppm)
428	6	405	16	562	190	39	4489	7.4	2590	0	23	0	2
418	5	436	13	1056	975	186	8812	6.4	6600	0	69	0	6
407	5	426	12	977	604	118	5444	7	5200	0	60	0	5
404	6	429	13	1076	887	163	7779	8.7	5220	0	69	0	6
438	7	458	16	611	444	90	3321	11.1	5490	1	39	1	11
387	6	439	13	921	391	73	5743	16	6100	0	27	0	8
388	4	441	11	705	118	24	3867	-1	2340	0	9	0	1
377	5	406	14	701	206	15	3775	2.4	1750	6	29	3	18
420	6	459	16	605	393	87	2713	9	6190	1	46	1	14
426	7	434	19	449	224	45	2371	12.5	4760	0	27	0	7
410	6	417	25	275	73	17	972	4.8	1670	0	8	0	2
425	5	480	17	534	476	101	1758	8.8	11400	0	55	1	19
374	5	428	24	482	122	23	937	19	1510	0	13	0	5
551	35	590	110	29	-1	0	144	1.9	370	0	0	0	0
414	4	416	19	573	363	68	3185	8.6	5150	0	23	0	6
419	5	400	33	309	26	7	1251	0.3	232	0	1	0	0
526	38	480	110	24	0	0	123	-1.1	194	0	1	0	0
485	10	531	52	137	6	1	411	-2.1	355	0	2	0	1
427	8	404	41	172	2	1	680	0.3	644	0	2	0	1
499	18	582	66	58	0	1	86	3.4	527	0	0	0	0
458	45	460	180	23	0	0	122	2.8	401	0	0	0	0
394	6	426	18	910	303	58	6439	2.5	3170	0	21	0	2
401	7	405	33	741	42	12	6957	3	960	1	2	0	1
415	6	418	25	754	360	72	9521	7	3430	0	25	0	5
408	5	407	19	959	441	88	5113	6	3200	0	24	0	3
466	18	429	48	183	5	2	19299	11	644	1	0	0	2
397	6	437	32	378	14	6	16560	2	650	1	1	0	0
381	5	416	38	260	5	2	-16980	11	922	0	2	0	1
409	4	409	27	483	204	42	553	5	2324	0	19	0	2
420	4	442	15	1108	916	189	7288	11	5300	0	56	0	7
414	5	432	20	758	256	53	-14909	4	3530	0	19	0	4
396	5	441	24	606	183	39	-6508	4	2580	0	13	0	2
405	5	446	20	712	456	89	-5444	4	4170	0	40	0	6

391	7	476	18	1357	472	97	5763	5	3600	0	24	0	3
402	5	443	23	715	134	29	-4350	7	2400	0	8	0	2
441	4	428	17	788	557	120	-15417	5	5620	0	42	0	9
434	2	432	14	1360	1128	247	9000	5	5960	0	75	0	8
431	4	441	16	1241	1170	260	7112	6	5200	0	57	0	7
394	3	442	21	827	150	34	4311	4	2550	0	8	0	3
436	4	463	19	1159	785	176	3172	4	3990	0	36	0	3
420	3	432	19	761	444	94	5905	4	4510	0	28	0	6
485	7	480	34	271	4	3	50088	47	1994	0	0	0	0
403	4	410	21	620	223	50	7803	4	2700	1	9	0	4
428	2	425	14	1356	1526	312	16543	5	5180	0	60	0	7
386	5	460	38	951	33	8	5637	12	502	0	1	0	1
429	5	424	9	902	701	143	10242	7	5300	0	45	0	5
443	4	413	12	400	227	48	3833	6	2753	0	25	0	3
422	4	425	11	524	353	73	5166	5	3400	0	31	0	4
423	5	422	12	543	308	63	2172	5	3070	0	26	0	3
427	4	409	7	1117	1344	257	2105	10	8650	0	68	0	7
997	9	978	16	97	76	35	22786	12	806	0	29	0	3
784	39	864	21	262	66	25	10600	8	620	1	21	0	2
1001	10	991	10	203	127	56	-14542	10	1078	0	36	0	3
978	10	992	13	97	45	20	-10914	9	438	0	21	0	1
1008	12	1006	17	69	45	20	-18200	12	499	0	20	0	1
415	4	427	10	643	705	135	4407	11	4310	0	28	0	5
408	4	437	12	521	175	36	8048	6	3710	0	14	0	5
447	6	414	15	298	146	30	2033	6	3120	0	17	0	4
424	4	426	12	554	438	87	10316	6	9970	0	29	1	14
947	7	998	7	762	311	137	11717	8	528	0	6	0	0
1304	15	1311	3	2650	935	536	42065	14	3350	0	22	0	3
1261	24	1274	5	2930	982	535	50074	17	3650	0	24	1	6
1149	8	1166	9	340	137	68	7653	8	1004	0	22	0	1
1475	12	1502	7	309	374	238	4150	11	4850	0	31	0	9
489	10	560	10	2610	438	80	6056	34	2640	6	61	8	58
1368	12	1319	8	283	156	108	3561	13	1318	1	22	1	12
1129	8	1155	6	632	174	90	10929	4	682	0	10	0	0
1165	8	1157	10	267	85	45	4230	2	542	0	7	0	0
1161	9	1179	7	463	131	71	11033	12	627	0	9	0	0

1712	12	1674	8	159	78	61	3743	2	1033	0	6	0	1
1584	13	1670	9	201	137	103	3010	3	1880	0	8	0	2
1695	15	1692	7	159	85	67	3597	2	1084	0	7	0	1
968	8	1004	12	186	77	35	730	13	469	0	13	0	0
1001	10	1000	16	239	93	45	2920	3	507	0	14	0	1
1480	12	1499	10	145	63	45	2823	3	1055	0	14	0	1
1413	13	1424	8	214	72	52	5794	3	807	0	12	0	1
1580	12	1659	4	1417	90	62	28833	14	823	0	2	0	0
477	6	443	23	172	107	24	1797	7	826	0	14	0	1
1312	10	1301	4	837	388	243	12975	12	1920	0	21	0	2
1289	14	1285	6	739	285	176	14913	6	1490	24	108	12	58
1337	10	1298	6	707	274	180	13785	34	1435	0	17	0	1
1134	13	1239	5	1455	639	381	43750	9	3000	0	18	0	5
882	55	988	32	753	130	72	8917	11	960	0	10	0	1
854	7	927	10	486	395	177	3638	20	3640	2	65	3	24
1366	15	1439	11	250	115	82	3788	8	884	0	23	0	3
1553	13	1549	8	421	6	4	9731	3	918	0	1	0	0
1010	9	946	8	536	270	128	5345	20	518	0	7	0	1
518	7	499	17	433	79	25	1688	7	1056	0	7	0	2
476	5	465	27	155	80	17	803	3	740	0	22	0	0
1207	12	1298	13	95	24	16	3955	4	894	0	4	0	1
1332	16	1322	18	70	20	13	1123	6	763	0	3	0	1
1507	15	1504	8	209	150	112	6190	11	936	0	25	0	2
1020	9	1019	11	230	54	26	2709	15	495	0	6	0	1
1010	8	1012	15	195	46	22	3510	12	518	0	6	0	1
919	10	929	14	182	56	23	2285	11	409	0	8	0	0
1430	14	1428	8	424	203	147	4408	8	3400	10	87	3	23
1674	20	1676	10	202	115	91	2873	3	1860	0	8	0	2
1719	27	1671	19	133	66	55	1566	2.3	1203	0	6	0	1
1490	14	1431	11	281	41	33	4376	2.7	878	0	4	0	0
921	19	925	16	398	125	54	-3400	3.8	324	0	10	0	0
991	15	1007	15	262	95	45	489	7.8	468	0	12	0	1
977	11	996	10	545	193	89	4545	8.1	627	0	14	0	1
984	10	1001	8	608	212	99	9475	10.3	615	0	14	0	1
924	21	954	16	523	241	101	5318	7.2	830	0	16	0	1
1272	14	1306	4	1484	883	523	5159	9.3	2790	0	30	0	3

1304	13	1289	7	1211	525	323	12814	7.2	2250	0	18	0	4
1043	35	1147	17	1948	1570	666	5307	16.7	4520	5	260	15	112
1334	16	1286	6	1248	623	396	13630	7.8	3180	0	20	0	5
1121	15	1216	7	1480	686	389	11854	8.4	3190	0	20	0	6
378	8	346	26	1028	7	1	4181	7.4	193	0	0	0	1
404	6	395	14	3020	820	135	6694	18.7	3030	15	400	25	180
1506	20	1486	13	259	261	189	4353	10.2	1960	0	36	0	5
1300	55	1427	20	336	234	165	4237	10.8	1870	0	41	0	3
1522	17	1466	12	277	190	141	4428	4.7	1710	0	42	0	3
906	16	997	15	706	50	12	8243	4.7	847	0	2	0	0
777	15	835	26	199	48	19	1195	9.6	508	0	8	0	0
880	21	872	26	165	49	19	1075	6.9	473	0	8	0	1
1333	22	1386	9	416	172	123	2856	8.5	3710	0	28	0	4
383	5	459	11	1429	16	5	3917	3.4	576	0	15	2	15
1210	12	1260	9	335	112	64	5623	9.8	1610	0	3	0	1
1202	14	1233	6	582	101	56	14765	5.3	1252	0	2	0	1
955	12	1002	7	718	55	25	6880	3.3	1268	0	7	1	6
375	4	439	11	950	4	2	3153	-0.7	238	0	4	1	7
1529	14	1540	5	495	266	197	11588	3.9	886	0	15	0	1
373	4	378	12	1010	4	1	4094	9.2	21	0	0	0	0
400	5	368	13	1337	31	6	4989	9.1	279	0	8	1	10
392	5	411	15	582	30	9	2347	29	520	0	5	0	3
404	5	406	19	356	58	10	1648	23.6	509	0	5	0	4
398	4	403	19	374	74	13	2243	32.6	805	0	8	0	7
384	4	384	10	2300	177	31	4883	38.9	698	2	17	2	18
773	12	813	12	295	106	39	4084	6.01	119	0	9	0	1
1412	14	1481	10	186	108	70	3830	4.4	1235	0	25	0	1
1527	14	1463	4	3763	1285	795	48465	11.1	1590	0	39	0	2
393	4	375	13	979	6	2	3623	2.2	11	0	0	0	0
837	7	937	9	639	321	128	8039	9.2	293	0	23	0	1
477	7	437	21	261	361	73	1783	9.2	1930	0	44	0	4
651	9	606	7	1090	522	146	13500	8.5	1728	0	19	0	5
374	4	423	18	494	7	2	1298	0.1	245	0	17	3	37
1269	20	1288	14	156	97	55	5021	16.5	1099	0	11	0	2
377	5	398	17	542	3	1	2346	2.8	37	0	0	0	0
1503	13	1539	8	228	80	56	3955	10.3	703	0	6	0	1

441	11	466	6	5030	235	45	17268	24.5	2530	7	111	11	82
533	5	564	10	797	754	183	6000	2.7	1180	0	27	0	1
1133	13	1260	7	751	83	57	10893	2.7	727	0	6	0	1
1299	10	1304	7	510	273	158	11690	11.2	1383	0	24	0	2
391	3	451	16	1294	10	6	2109	280	120	0	7	1	8
382	3	439	12	2248	12	8	2864	1530	165	0	7	1	11
397	4	457	13	1625	32	14	4115	6.1	180	0	10	1	11
394	4	408	10	1340	9	4	2770	276	68	0	9	1	7
366	3	420	18	715	47	9	2486	238	505	0	6	0	3
707	10	781	12	357	207	76	3872	14.7	594	0	18	1	4
1327	14	1315	11	210	100	63	4570	9.3	845	0	14	0	1
602	5	581	12	655	798	221	3791	5.1	955	0	68	0	2
561	4	545	10	1156	1691	472	7353	6.9	1022	0	120	0	3
365	5	386	19	482	4	1	1147	1	124	1	12	1	7
414	5	392	10	1331	270	56	5718	11.9	1004	0	17	0	1
393	4	403	14	797	65	17	4316	5.8	383	0	6	0	1
950	10	995	5	1894	123	53	50077	8.6	1194	0	6	0	3
981	11	988	14	150	39	18	3159	7.2	531	0	17	0	0
1006	16	1032	31	41	18	7	617	8.4	692	0	9	0	2
1019	12	1009	11	273	87	44	5270	9.5	507	0	14	0	1
435	4	507	15	593	13	7	2764	2.7	95	0	2	0	0
1038	11	1017	11	265	92	47	3518	10.5	543	0	14	0	1
1031	11	1017	9	389	134	69	5716	8.2	631	0	16	0	1
1660	16	1672	10	131	84	70	3728	6.3	1249	0	8	1	14
1021	8	1006	8	557	14	8	5408	8.7	2480	0	4	0	0
998	11	992	6	778	18	10	7208	3.9	1910	0	5	0	0
1039	8	1050	5	1276	13	6	22805	5.8	733	0	2	0	0
936	8	929	7	884	9	4	10172	7.2	306	0	0	0	0
1536	18	1487	6	463	7	6	9396	6	382	0	1	0	0
1580	24	1529	8	272	86	58	7095	4.8	1044	0	10	0	2
1593	20	1592	7	466	880	590	5830	14.3	3510	0	62	0	11
1454	18	1492	7	416	12	5	9056	4.4	305	0	1	0	0
921	9	952	13	276	64	30	6895	6.8	464	0	20	0	1
583	7	569	19	300	87	27	3428	18	244	0	2	0	1
405	3	408	10	1176	66	14	4481	5.4	866	0	1	0	2
1081	14	1176	9	495	489	287	10384	47	1970	0	19	1	10

898	8	932	5	2066	165	82	33870	16.1	479	0	34	2	21
417	13	466	32	1413	209	45	9727	6.4	970	0	1	0	0
628	7	665	11	773	614	172	2454	8.8	940	3	126	20	153
395	4	472	15	637	53	12	4086	6.6	531	1	26	3	15
962	11	945	18	195	44	22	2751	6.6	609	0	12	0	1
1534	18	1557	10	141	76	58	835	12.7	518	0	11	0	1
1569	15	1532	7	277	163	130	8651	6.5	880	0	13	0	2
1537	16	1547	7	227	264	203	7533	9.7	2940	0	33	1	11
470	5	440	22	277	174	39	4231	5.2	2110	0	57	0	2
472	5	486	16	274	213	49	2010	6.9	2370	0	68	0	2
463	5	449	13	477	370	81	4383	8.2	3580	0	116	0	3
474	6	464	17	410	423	97	4907	11.3	3820	0	126	0	5
470	5	447	20	324	232	52	2700	7.3	2210	0	51	0	3
478	5	432	16	323	345	77	551	6	3260	0	80	0	7
1328	13	1278	10	182	87	57	8170	10.8	1072	0	11	0	1
398	5	479	17	680	82	20	2404	384	1240	0	6	1	4
453	7	452	9	1242	236	58	11824	8.7	2280	0	32	1	4

Sm (ppm)	Eu (ppm)	Gd (ppm)	Tb (ppm)	Dy (ppm)	Ho (ppm)	Er (ppm)	Tm (ppm)	Yb (ppm)	Lu (ppm)	Hf (ppm)
8	1	45	19	228	86	433	91	860	171	9160
19	1	117	46	571	212	890	172	1510	279	10700
15	1	97	37	498	183	789	157	1500	314	10960
17	1	115	40	532	198	794	154	1370	248	10350
26	2	122	46	588	223	910	175	1490	287	10300
16	1	96	38	470	191	860	191	1970	491	12100
5	0	30	12	157	70	390	105	1180	343	12580
11	1	22	8	131	64	367	99	1144	270	9690
28	2	118	46	550	201	948	183	1540	310	9100
18	1	97	37	473	181	757	159	1540	311	9780
4	1	26	11	144	60	307	65	685	154	9390
46	5	250	93	1082	386	1570	320	2700	466	8350
4	1	20	9	107	46	281	74	870	238	12200
0	0	1	0	9	9	87	38	660	211	13000
15	1	90	40	472	182	892	170	1570	312	9200
1	0	4	2	22	7	31	6	60	17	13370
0	0	0	0	6	5	50	22	379	115	13240
1	0	1	1	13	9	78	30	490	149	13450
0	0	1	1	21	17	156	58	948	281	13800
0	0	0	1	16	13	131	52	876	276	12340
1	0	0	0	10	10	109	44	781	217	14030
7	1	48	23	294	117	580	130	1390	316	10320
2	0	3	2	26	22	223	107	1660	429	9870
14	1	67	25	304	124	569	118	1140	242	10800
7	1	46	19	255	101	500	123	1300	260	10190
2	1	8	5	44	19	113	41	570	169	9200
1	0	1	1	16	16	174	90	1350	366	10480
2	0	13	4	48	26	223	99	1530	452	10900
4	0	35	15	176	80	379	84	897	178	10100
17	1	111	41	480	184	782	158	1460	265	9560
9	1	59	24	288	122	600	131	1270	262	10070
8	1	47	18	210	84	423	110	1250	261	10560
14	1	79	33	407	164	679	139	1290	257	10710

5	1	51	19	258	110	570	158	1840	410	10060
5	1	30	11	144	66	419	137	1990	497	10960
19	1	117	43	525	190	854	174	1524	272	9840
19	1	129	49	568	218	930	177	1681	310	9520
16	2	104	38	460	171	780	185	1570	309	9540
4	1	31	12	156	80	490	159	2260	546	10960
9	1	71	29	349	134	643	145	1280	230	10120
14	1	89	32	381	140	606	134	1300	256	9720
2	2	21	9	105	55	424	158	2270	561	11230
9	1	51	18	227	95	513	132	1540	322	9400
16	1	109	41	469	191	778	158	1469	264	11060
1	0	6	2	22	13	110	42	780	194	10900
13	1	95	36	432	168	752	153	1280	233	16500
7	1	54	19	243	99	427	91	819	150	15440
10	1	67	24	281	115	507	101	884	163	12600
8	1	64	22	275	106	476	101	908	170	15980
20	2	148	51	595	229	966	193	1650	298	10200
5	1	23	8	86	30	128	27	252	49	11300
3	0	13	5	57	21	99	24	255	54	18110
5	1	26	9	97	36	160	36	327	65	16950
1	0	9	3	38	15	69	16	154	33	15900
2	0	10	3	44	17	72	16	164	33	14500
12	2	95	33	401	158	699	131	1103	205	8520
12	1	77	27	328	131	631	139	1441	281	10200
9	1	67	23	275	112	489	100	890	169	11500
27	3	174	58	697	264	1073	214	1800	321	8230
1	0	7	3	34	16	80	21	217	50	10210
9	0	55	21	282	115	518	113	1010	205	13900
12	1	60	22	300	116	531	119	1062	226	14720
2	0	15	6	74	32	156	35	338	78	10270
21	3	120	36	431	152	663	129	1127	235	7990
56	8	102	25	223	77	367	97	1096	314	20400
19	1	52	13	135	47	199	40	378	74	10280
1	0	10	4	51	21	104	23	224	48	12960
1	0	10	3	45	19	83	18	179	38	10810
2	0	10	4	52	20	98	20	194	42	11940

3	0	20	7	92	37	166	35	327	70	9420
7	1	44	15	176	66	285	55	519	104	9260
3	0	20	7	94	35	164	36	336	70	9420
2	0	10	3	38	15	73	16	165	34	11390
2	0	10	3	43	16	73	17	164	37	11800
3	0	22	8	99	39	162	33	312	65	10560
3	0	17	5	72	27	124	28	267	55	10730
2	0	10	4	53	26	137	33	348	78	12700
3	1	18	6	72	30	136	29	278	59	9490
6	0	37	14	170	67	294	62	580	110	11450
32	3	65	18	162	52	221	46	435	80	11690
4	0	26	10	126	50	219	48	445	95	11140
14	1	65	23	288	104	476	88	796	160	10900
3	0	16	6	79	33	170	39	425	105	10700
32	2	101	30	339	126	524	105	885	181	8710
5	0	18	6	78	32	134	25	240	43	13060
0	0	5	3	56	29	180	55	680	154	13700
1	0	7	3	35	16	81	19	224	53	11640
3	1	18	6	77	34	173	48	537	124	9900
1	0	8	3	57	24	126	28	285	62	13330
2	0	16	6	73	31	132	29	287	67	9090
3	0	16	6	72	29	132	27	244	54	9340
6	1	21	8	82	32	139	29	269	57	10900
2	0	11	4	45	18	77	15	141	30	12730
2	0	13	4	48	17	74	16	139	28	12100
1	0	7	3	37	14	70	14	145	33	11880
20	3	95	28	313	117	518	101	922	178	7110
6	1	41	15	180	65	305	57	533	99	9600
3	0	22	9	112	45	189	37	351	69	9410
1	0	13	5	70	28	140	30	300	67	11760
1	0	4	2	24	10	53	13	138	27	10750
1	0	8	3	39	15	79	16	172	33	11860
1	0	10	4	48	21	112	23	238	51	13050
2	0	9	4	45	19	104	23	255	49	12150
2	0	13	6	67	26	136	30	293	62	12060
7	0	53	19	228	94	408	78	757	144	10800

7	0	49	17	201	83	381	76	703	137	13430
140	42	230	61	540	167	700	130	1190	220	11190
12	0	75	24	303	109	481	89	817	148	10040
14	1	71	25	298	114	508	96	861	169	11340
1	1	6	2	17	5	17	4	26	4	12800
50	11	96	23	248	89	490	118	1420	348	13600
8	3	50	16	180	62	293	55	528	104	9130
8	2	46	15	170	69	300	56	578	121	9970
6	2	38	12	137	54	266	54	531	105	9460
1	0	8	4	57	26	145	32	386	76	11650
1	0	10	4	41	17	84	17	178	39	12060
1	0	11	3	39	16	74	15	165	31	11070
11	2	99	30	351	137	565	110	1058	194	7900
13	1	24	3	27	17	140	49	710	202	10390
5	0	31	12	150	56	247	52	467	94	10990
3	0	22	8	110	41	189	42	405	80	11910
5	2	19	7	93	36	178	39	355	69	13970
6	0	10	2	14	7	62	27	507	157	12500
2	1	15	5	63	26	134	32	338	81	11720
1	0	3	1	4	1	1	0	3	1	12800
9	2	18	3	20	7	57	20	325	95	11520
2	0	4	1	21	9	81	22	360	113	12400
7	2	22	4	40	15	74	20	199	44	12270
15	5	38	7	70	24	121	25	237	48	11240
18	7	59	10	69	24	108	23	222	45	12100
2	0	5	1	12	4	16	3	44	10	8640
4	0	23	9	106	42	196	42	392	83	10370
4	2	23	8	102	40	202	47	480	102	11780
0	0	3	1	3	0	1	0	2	1	12200
2	1	7	2	23	9	51	14	179	42	11870
6	2	42	15	172	64	295	62	552	112	8530
8	1	37	12	151	56	264	58	488	104	10580
30	1	55	7	35	8	34	12	204	62	12060
4	1	26	9	108	40	170	35	312	65	8850
0	0	5	1	4	1	6	1	21	6	13020
1	0	12	5	59	23	112	24	217	44	11360

41	9	67	19	209	73	414	115	1422	361	12200
3	1	18	6	91	35	195	46	473	111	12100
2	1	11	4	51	21	108	25	268	64	10230
5	0	28	10	116	45	203	44	400	77	11900
6	1	20	3	18	4	11	2	15	4	12130
8	1	18	4	26	5	15	2	15	3	11490
12	1	25	5	25	5	17	3	22	5	11540
7	1	18	3	16	3	6	1	7	2	12100
5	3	22	5	44	16	70	16	157	39	8970
3	2	11	3	50	20	96	24	267	66	9040
2	0	14	5	64	26	119	26	256	47	9710
4	2	23	7	81	30	138	27	277	64	8870
5	3	31	9	93	30	138	27	254	57	10030
3	1	6	2	12	4	18	4	33	12	12390
2	1	13	5	68	30	181	46	541	132	12720
2	0	9	3	34	12	57	14	139	29	11600
5	1	23	10	119	38	152	27	240	44	14210
2	0	10	3	43	17	74	17	168	33	11300
4	1	18	6	68	23	96	20	177	36	8350
2	0	10	4	50	19	80	17	160	29	13270
0	0	3	1	8	3	13	3	27	6	12110
2	0	12	4	53	19	83	16	163	29	13130
2	0	14	4	54	19	91	19	179	35	13300
15	2	43	11	125	44	188	37	334	67	8280
2	1	24	13	189	82	435	119	1241	257	12400
2	0	18	10	164	69	381	101	1188	249	12210
0	0	2	2	33	20	154	47	578	175	13250
2	0	13	5	38	10	31	5	35	6	14200
0	0	1	1	15	9	65	20	233	61	12640
4	1	18	6	78	35	163	38	381	91	10050
22	4	103	33	370	145	610	124	1030	211	8950
0	0	1	1	15	8	56	17	193	50	12400
2	0	6	2	33	14	71	20	213	54	12130
4	0	14	4	28	8	27	6	58	14	13180
2	0	7	3	52	26	153	40	462	119	14350
12	5	57	16	186	72	306	63	592	110	9110

23	3	42	7	56	16	64	13	107	20	9220
1	1	8	3	48	29	212	69	990	277	14600
130	10	147	17	118	33	131	30	288	57	10980
5	3	12	3	36	16	93	27	381	105	13520
2	0	11	4	51	21	91	21	211	48	10880
1	0	10	3	41	17	78	17	171	38	12900
3	1	19	6	82	30	120	27	257	53	12680
13	1	82	24	261	99	388	72	684	131	10700
4	2	35	12	164	69	297	64	662	141	11670
6	4	47	15	209	83	378	78	734	158	9610
8	5	63	24	296	121	532	111	1024	230	10200
11	6	88	29	337	131	578	109	1065	229	9760
7	4	49	17	216	79	338	69	649	140	10010
13	7	94	28	333	120	472	92	934	189	10940
3	0	21	7	89	35	155	34	290	61	9240
4	1	23	8	97	41	212	51	581	161	12500
6	1	43	17	210	82	412	100	1160	290	10780